

Journal of Geophysical Research: Planets

RESEARCH ARTICLE

10.1029/2017JE005448

Key Points:

- Map patterns and topographic expressions are consistent with basement-block-style faulting analogous to intraplate thrusting on Earth
- Thrust fault-related landforms show a high variability in amount and along-strike distribution of structural relief
- Along-strike relief variations inform fault growth behavior to include restricted and unrestricted growth, fault interactions, and linkage

Correspondence to:C. Klimczak,
klimczak@uga.edu**Citation:**Klimczak, C., Kling, C. L., & Byrne, P. K. (2018). Topographic expressions of large thrust faults on Mars. *Journal of Geophysical Research: Planets*, 123, 1973–1995. <https://doi.org/10.1029/2017JE005448>

Received 13 SEP 2017

Accepted 1 JUL 2018

Accepted article online 10 JUL 2018

Published online 9 AUG 2018

Topographic Expressions of Large Thrust Faults on Mars

Christian Klimczak¹ , Corbin L. Kling^{1,2} , and Paul K. Byrne² ¹Structural Geology and Geomechanics Group, Department of Geology, University of Georgia, Athens, GA, USA, ²Planetary Research Group, Department of Marine, Earth, and Atmospheric Sciences, North Carolina State University, Raleigh, NC, USA

Abstract On planets with little erosion, thrust faults produce broad, asymmetric, positive-relief, linear to arcuate ridges—often referred to as lobate scarps—that remain largely unaltered, such that their topographic expressions are a measure of the structural uplift caused by the displacement and associated country rock deformation of the faults. Here we map and systematically assess the structural relief of 24 thrust faults across Mars to infer their growth behavior. Our mapping indicates that the majority of individual thrust faults have simple, linear map traces with lengths of up to ~450 km but that some thrust faults form systems of up to 1,400 km in length. For the most topographically pronounced landforms, the structural relief developed above the fault is as great as ~3,400 m. We then relate topographic measurements to the displacement on the underlying fault planes to study the displacement variations along the fault length. We find a variety of displacement distribution shapes of the fault systems, which we attribute to differences in fault growth that include unrestricted and restricted growth, linkage, and/or fault interaction. Finally, we relate the maximum displacements (D_{\max}) determined for each of the faults to their respective fault length (L) to establish a maximum displacement-to-length relationship. The observed scaling characteristics and order-of-magnitude scatter of our D_{\max}/L data are not uncommon for fault populations on Earth and tie in well with the map patterns, tectonic geomorphology, and systematic along-strike displacement distributions to have grown in a basement-block faulting style found in intraplate tectonic settings on Earth.

1. Introduction

1.1. Thrust Fault-Related Landforms on Mars

Thrust faults are fracture surfaces in planetary lithospheres along which shortening is accommodated. The portion of the faulted rock mass above the fault plane (the hanging wall) is displaced over the portion of the rock mass below the fault plane (the footwall), forming positive structural relief. As is typical for any large-scale fault on Earth, thrust fault systems on Mars likely consist of complex zones of deformation involving one or more fault planes (e.g., Johnson, 1995), a zone of intensely sheared rock referred to as the fault core (e.g., Caine et al., 1996), and a fault damage zone (e.g., Kim et al., 2004) surrounding the fault core. Yet insight into fault zone complexity and fault rock properties on Mars is limited, and so large faults are generally approximated as one large slip plane (Figure 1).

The surface of Mars abounds with landforms that are interpreted to be underlain by thrust faults (e.g., Chicarro et al., 1985; Knapmeyer et al., 2006; Watters, 1993). Because of low rates of erosion and degradation of topography on Mars (Golombek & Bridges, 2000), the accommodated strain and deformation associated with these landforms and their underlying fault have been preserved for billions of years. Surface-breaking thrust faults on Mars have landforms with asymmetric ridges, with one steep-sloped cliff facing the direction of tectonic transport and a gentler slope dipping in the same direction as the underlying fault plane (e.g., Schultz, 2000; Schultz et al., 2010; Schultz & Watters, 2001; Watters, 2003a; Figure 1). On the basis of structural arguments for thrust faults on Earth, these ridges are widely interpreted to represent some combination of fault-propagation folds (anticlines) and fault displacement-gradient folds (e.g., Suppe & Medwedeff, 1990; Wickham, 1995) that formed as a consequence of accumulation and variations in slip along the fault. Decreases in cumulative slip toward the fault tips are compensated by buckling of material above the fault (Mitra, 1990; Suppe & Medwedeff, 1990; Williams & Chapman, 1983).

Topographic signatures of numerous thrust fault examples have been characterized in cross section with topographic transects across the landform (e.g., Watters et al., 2000; Watters & Robinson, 1999). The topographically most pronounced thrust fault-related landforms are located in the southern highlands of Mars (Watters, 1993), whereas most such landforms in the northern lowlands are generally

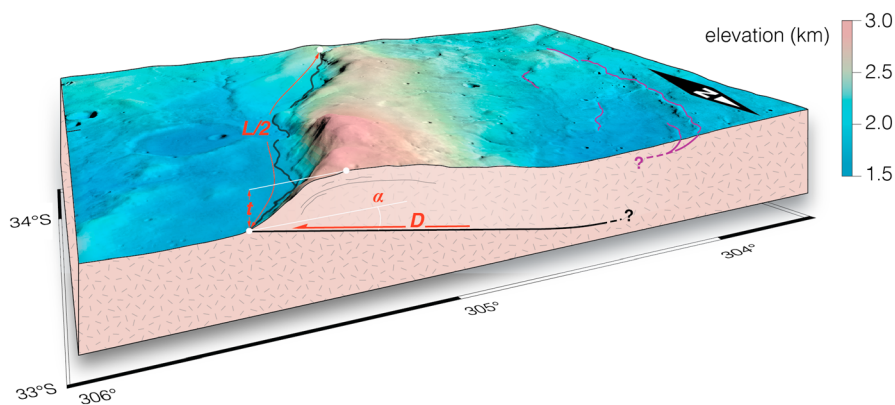


Figure 1. Block diagram of Ogygis Rupes plotted using a THEMIS image mosaic overlaid with MOLA topography, showing this ~181-km-long, topographically pronounced thrust fault-related landform in the southern hemisphere of Mars. The surface break of the main fault is mapped in black; smaller thrust fault-related landforms are mapped in dark purple. Fault-geometric properties include fault length, here shown as the half-length ($L/2$), fault displacement (D), the vertical component of displacement (fault throw, t), and the fault dip angle (α).

less physiographically prominent. Based on morphological characteristics, thrust fault-related landforms on Mars have traditionally been termed *lobate scarps* and *wrinkle ridges*. However, this classification scheme breaks down in many cases due to the large variability of the shape of these landforms (cf. Byrne et al., 2014), and thus, these terms are not used here.

The topographic signatures of Martian thrust-fault-related landforms have been related to the subsurface fault geometry (e.g., Okubo & Schultz, 2004; Schultz, 2000; Schultz & Watters, 2001), and numerical simulations of surface displacements have been matched to individual topographic profiles measured across given landforms to estimate fault dip, displacement, and penetration depth (e.g., Egea-González et al., 2017; Grott et al., 2007; Mueller et al., 2014; Ruiz et al., 2008; Schultz & Watters, 2001; Watters, 2004). One of the longest and topographically most pronounced landforms on Mars, Amenthes Rupes, has received the most attention in the scientific community (Mueller et al., 2014; Ruiz et al., 2008; Schultz, 2003a; Schultz & Watters, 2001; Watters et al., 2000). This landform has a length of ~420 km, shows a topographic relief in excess of 1,000 m along much of its length, and its underlying fault system is found to penetrate the Marian lithosphere to 30 km (Schultz & Watters, 2001) or even as much as 48 km (Mueller et al., 2014).

Studies modeling subsurface fault architecture considered only a few such landforms, and for each of the modeled structures, only a single or, at best, a few topographic profiles over a limited geographic region informed the numerical solutions. Nonetheless, modeled fault-geometric parameters were used to infer not only the amount of brittle strain accommodated by thrust faults on Mars (Schultz, 2003b) but also the depth and rheological properties of the Martian lithosphere (e.g., Ruiz et al., 2008; Schultz, 2003a) as well as regional heat flow (Egea-González et al., 2017; Grott et al., 2007; Mueller et al., 2014; Ruiz et al., 2008). These results have also been used as a basis from which to obtain global insight into the seismic environment on Mars (Knapmeyer et al., 2006), as well as the amount of radius decrease the planet may have experienced from contraction arising from secular interior cooling (Nahm & Schultz, 2011).

1.2. Geometry and Growth of Thrust Faults

Thrust faulting on Earth occurs in different geometric styles. The spectrum of geometries ranges from thrust belts that are typically found in orogenic settings to basement thrusting that typically occur in intraplate, continental settings. Thrust belts are characterized by multiple, subparallel, long, sinuous thrust traces (e.g., Ray, 2006), involving imbricate thrust systems, which can be surface-breaking or blind. Duplex structures, which commonly form with this structural style, have horizontal floor and roof thrusts (Boyer & Elliott, 1982), along which large amounts of strain are accommodated. These complex structures are in stark contrast to basement thrusts that typically consist of a single major fault with one or only a few segments forming relatively simple linear map traces and accommodating strain by block faulting. For this structural style, the majority of deformation is localized in a narrow zone along the major fault (e.g., Matthews & Work, 1978). Irrespective of

the faulting style, thrust faults produce positive-relief landforms, and so landform shape and the associated vertical relief provide a first-order measure of the displacement of the fault.

Although correlation between landform or fold shape and its underlying fault is found to be nonunique for many numerical models (e.g., Hardy & Finch, 2005; Schultz & Watters, 2001; Zehnder & Allmendinger, 2000), certain aspects of thrust fault geometry on Mars can be directly inferred from the shape of their respective landforms, especially for landforms that show clear surface breaks. These fault geometric properties include fault length (L ; Figure 1), the azimuth of the mapped fault trace (which approximates the strike of the fault plane), and the fault dip direction (which is suggested by the gentle slope of the landform that formed above the fault; Figure 1).

Additional information on the fault may be obtained by studying the structural relief of the landforms preserved in the hanging wall of the fault, although information obtained from such measurements must be carefully interpreted. Although field observations (Lavé & Avouac, 2000; Burgess et al., 2012), 3-D seismic studies (e.g., Apotria & Wilkerson, 2002; Lohr et al., 2008; Shaw et al., 2002, 2005), and modeling (e.g., Hardy & Finch, 2005; Zehnder & Allmendinger, 2000) for thrust-belt-style faulting indicate that fault displacements (D) may not be accurately determined by assessments of hanging wall deformation alone, displacements accommodated along basement faults are closely related to the structural relief produced by the fault. Thus, first-order assessments of thrust fault displacements on Mars must be placed into the context of the structural styles of thrust faulting interpreted from map patterns and landform morphology.

Under the assumptions that the structural style of faulting does not drastically change within a single landform, and that the topographic expressions of the landforms to first-order represent some measure of fault displacement, assessments of variations in structural relief along-strike the faults may offer insights in variations of the vertical component or throw (t) of the fault displacement of the thrust system (especially if hanging wall deformation is minor). With knowledge of the dip angle (α) of the fault plane (measured from horizontal), and how that value may vary with depth (i.e., a fault plane that is planar [or homoclinal] versus curved [or listric]), fault displacement may be inferred from fault throw (see section 2 for assessment of fault dip).

The fault length is measured as the length of the fault surface break and so it is obtained by carefully mapping the landform in plan view (Figure 1). Faults may not always have single surface breaks, but commonly occur in en echelon arrays, where multiple, closely spaced and overlapping fault segments form the overall structure (e.g., Dawers & Anders, 1995; Willemse, 1997). Fault overlap and underlap (the horizontal distance between two parallel fault segments as measured parallel to the strikes of the faults), as well as fault spacing (the horizontal distance between two fault segments as measured perpendicular to the strikes of the faults), are additional key parameters that can be measured from the map patterns of fault systems (see Figure 1 in Willemse, 1997).

Faults are three-dimensional structures, and so variations in shape of the landforms along their lengths provide insights into the subsurface architecture and growth geometry of the fault itself. The methods commonly used to gain such insights are best suited for field observations collected in tectonic settings that allowed the faults to develop, grow, and remain preserved without major tectonic overprint, such is typically the case in intraplate settings or at divergent plate margins. Fault growth results in longer faults having greater maximum displacements than shorter faults (Clark & Cox, 1996; Cowie & Scholz, 1992b; Gillespie et al., 1992; Marrett & Allmendinger, 1991; Walsh & Watterson, 1988; Watterson, 1986). In particular, fault length (L) is found to scale with fault displacement (D) in the general form of

$$D = \gamma L^c, \quad (1)$$

where γ is the scaling coefficient and c is the scaling exponent. The scaling coefficient is related to host rock strength and shear modulus, the (elliptical) shape of the fault plane, and the driving stress conditions acting on the faults of the given population (Schultz et al., 2006; Schultz & Fossen, 2002), whereas the scaling exponent is indicative of the fault shape evolution within the population (see details below). Displacements are often expressed as either maximum or average displacements. In the remainder of this manuscript, we use the maximum displacement (D_{\max}).

Fault lengths may scale to their displacements in either a linear (e.g., Clark & Cox, 1996; Cowie & Scholz, 1992b) or a nonlinear manner (e.g., Gillespie et al., 1992; Marrett & Allmendinger, 1991; Walsh & Watterson,

1988; Watterson, 1986). Linear scaling is achieved when the scaling exponent assumes unity ($c = 1$) and reflects self-similar fault growth. Self-similarity also predicts that small and large faults form with similar along-strike displacement distributions. Along-strike displacement distributions typically show the lowest displacement values near the fault tips and highest near the center of the fault. Unrestricted (or uninhibited) fault growth, where the fault grows without confinement to a mechanical layer or interaction with other faults, results in an overall symmetrical and peaked along-strike distribution of displacement, with maximum displacements located at or near the fault center (Cowie & Scholz, 1992a, 1992b; Dawers et al., 1993; Manighetti et al., 2001; Walsh & Watterson, 1987).

Non-self-similar fault growth leads to power law scaling exponents above or below unity. Exponents below unity, in particular, are commonly found. They are indicative of either fault interactions and fault growth by linkage (Cartwright et al., 1995; Schultz et al., 2010; Wyrick et al., 2011) or confinement of the fault to a mechanical layer (Dawers et al., 1993; Polit et al., 2009; Schultz & Fossen, 2002; Soliva et al., 2005; Soliva & Benedicto, 2005). Either process promotes a systematic increase in the fault aspect ratio (Schultz & Fossen, 2002): the fault length increases *without* a proportionate increase in displacement. As a consequence, displacement distributions may show asymmetric or flat-topped (i.e., plateau shaped) along-strike displacement distributions (Dawers et al., 1993; Manighetti et al., 2001; Polit et al., 2009; Soliva et al., 2005, 2006; Soliva & Benedicto, 2005).

Interaction and linkage of faults in en echelon arrays can be distinguished from fault confinement by measuring and evaluating spacing and overlap of the different fault segments (e.g., Soliva et al., 2006; Soliva & Benedicto, 2005). Both parameters can be obtained by photogeological mapping. Under a scenario where the overlap-to-spacing ratio between en echelon fault segments is sufficiently large, usually for ratios of 1 to 4 (e.g., Willemse, 1997), and where displacement distributions are found to be asymmetric with maximum displacements skewed toward the overlapping fault tips (Dawers & Anders, 1995; Willemse et al., 1996), faults can be assumed to have mechanically interacted. This interaction occurs even for faults that are not physically connected, through local perturbation of the stress field at the fault tip (Willemse, 1997). Such fault interaction is referred to as *soft linked* (e.g., Walsh & Watterson, 1991), whereas faults that have coalesced and thus are physically connected are termed *hard linked* (e.g., Trudgill & Cartwright, 1994).

1.3. Aims of This Study

Here we investigate with detailed mapping and topographic measurements the shapes of a set of thrust fault-related landforms across Mars (Figure 2). From our analysis we characterize the map pattern, fault length, displacement distribution, and maximum displacement for each of the faults and fault systems. With assessments of these parameters for a series of structures across the surface of Mars, we aim to (1) identify if displacement distributions of thrust faults on Mars yield systematic results that would allow us to study fault growth, and, if so, (2) interpret and assess the variability of thrust fault displacement distributions to infer how thrust fault growth is expressed on Mars, as well as (3) deduce the style of faulting from map patterns to evaluate possible processes responsible for thrust faulting.

2. Data Collection

Our structural mapping was carried out with the 100 m-per-pixel (m/px) THEMIS daytime mosaic (e.g., Edwards et al., 2011), complemented with ~10 m/px images from the Mars Express High Resolution Stereo Camera (HRSC; Neukum et al., 2010) and ~6 m/pixel images from the Mars Reconnaissance Orbiter (MRO) Context Camera (CTX; Malin et al., 2007). Fault topography was assessed with the Mars Orbiter Laser Altimeter (MOLA) global digital elevation model, which has a ±3 m vertical resolution and a minimum spatial resolution of 463 m/px at the equator—well suited for large, topographically pronounced thrust faults such as those we examined.

The faults were mapped in ArcMap© 10.2 as polyline shapefiles at a mapping scale of 1:1,000,000. The mapping scale was increased to 1:250,000 to facilitate more precise mapping of finer structural detail as required. Our mapping approach involved tracing the surface break of the most topographically pronounced landforms of each region of interest, recording smaller landforms with surface breaks associated with the major landform, and identifying broad ridges with no clear surface break, similar to those mapped in Mare Crisium on the Moon (Byrne et al., 2015). The streaming function in ArcMap was used

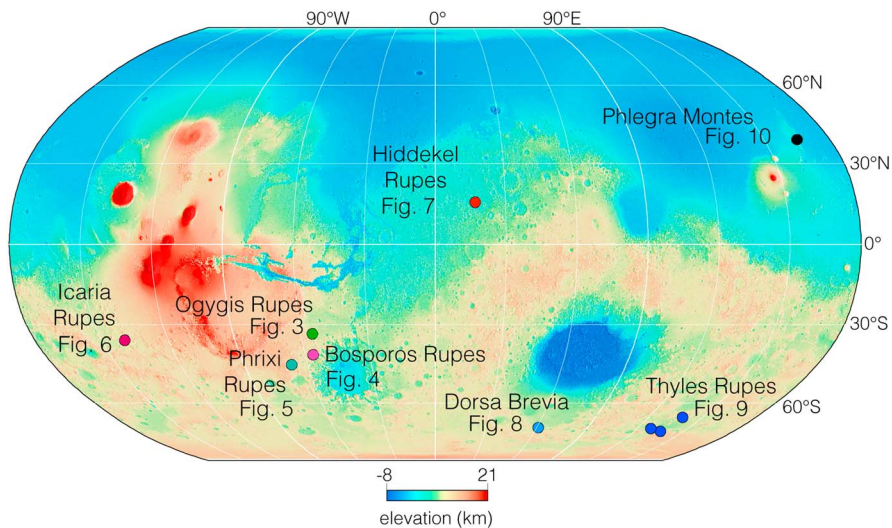


Figure 2. Global, color-coded MOLA map of Mars in Robinson projection showing the geographic distribution of the studied thrust fault-related landforms. The locations of landforms are indicated by colored points that correspond to colors for fault systems in subsequent figures.

to evenly place nodes every 500 m along the surface trace of the fault. Once mapping was complete, geodesic values of the length of the mapped fault traces were derived with the “Tools for Graphics and Shapes” plugin for ArcMap, which minimizes length distortions from projected data sets (http://www.jennessent.com/arcgis/shapes_graphics.htm).

We refer to fault surface breaks identified as continuous map traces on the scale of our mapping as *single* or *individual* faults, although we recognize that segmentation of such single faults may exist on finer scales. Furthermore, faults or landforms were considered as *large* or *major* when their lengths were found to likely be greater than the thickness of the brittle lithosphere (e.g., Cowie & Scholz, 1992a).

Topographic information was extracted from the MOLA elevation model by placing transects orientated perpendicular to the mapped fault traces at ~10 km intervals. These topographic transects were used to find the difference in elevation between the base and the top of the thrust fault-related landform, yielding a measurement of the preserved structural relief. The relief measurements were cross-checked with the photogeology to ensure that all values were recorded as an accurate representation of the total structural relief of the fault. Doing so was especially important where impact craters superposed a fault scarp, for instance, or in complex fault systems where multiple landforms were present within a single topographic profile.

Because of erosion rates of less than 1 nm/year on the Martian surface (Golombek & Bridges, 2000), and given that inclined fault planes underlie the landforms, we interpreted the structural relief to correspond closely to the throw of the studied thrust faults (see section 1.2 for details). The throw values for a given fault were plotted at their measured position along the length of that fault to obtain a throw distribution profile for the structure. For systems where multiple faults were present, cumulative throw distribution profiles were obtained from individual faults by summing the throw values in areas where faults overlapped. Cumulative throw values were also plotted as a function of their position along the length of their corresponding fault system to show total throw accumulation. Where a fault throw could not be readily identified (e.g., where a crater had erased preexisting fault-related topography), fault throws were interpolated between the two closest possible measurements. At the mapped fault tips, the fault displacement was assumed to reach zero, as no fault-related topography could be detected in those locations at the resolution of the MOLA data set.

Finally, the maximum measured throw value for each fault and fault system was identified. These maximum throw values can be used to estimate the maximum fault displacement (D_{\max}) using a simple trigonometric relationship between throw, dip angle (α), and displacement, such that $\sin \alpha = t/D_{\max}$. Additionally, the prediction for frictional sliding when considering the frictional properties of a basaltic rock mass, such as the Martian lithosphere, indicates that slip is promoted along planes with an optimal angle of ~30° to the

direction of the most compressive tectonic stress (Jaeger et al., 2007). Because thrust faults typically form when the most compressive stress component is horizontal (Anderson, 1942), this angle corresponds to a dip of 30° for thrust faults. Although low-angle normal faults or high-angle thrust faults are not explained by the optimum angles for frictional sliding, dip angles in the range between 20° and 40° derived from numerical modeling of thrust fault subsurface architectures on Mars (e.g., Egea-González et al., 2017; Grott et al., 2007; Mueller et al., 2014; Ruiz et al., 2008; Schultz & Watters, 2001) are in good agreement with predicted dip angles for thrust faults. Following these considerations, we estimate the maximum displacements of the thrust faults in this study for dips of 30° with a ±10° uncertainty.

The derived maximum displacements for each fault were then plotted against their respective length value to determine the corresponding displacement-length statistic. Given that some modification of topography may have taken place, that fault dips are generalized, and considering variable hanging wall deformation of individual thrusts, the numerical values of the individual measurements of throws and D_{\max} derived here may include multiple sources of uncertainties. However, as stated above, assessments of systematic variations (irrespective of the numerical values of the individual measurements) of fault throw and throw maxima allow for first-order assessments on fault growth and fault scaling that are representative of the geometry and growth history of these structures.

3. Descriptions of Thrust Fault-Related Landforms

3.1. Ogygis Rupes

Ogygis Rupes, centered at 33.0°S, 54.5°W, is a 181-km-long thrust fault-related landform (Figure 3). The mapped fault surface break is curvilinear and consists of two clearly visible fault segments. The southern fault segment is 40 km long, and its surface break terminates at the 150-km-long northern segment, displaying a branch point (e.g., Boyer & Elliott, 1982). The two segments have an overlap of ~10 km and a spacing of less than 1 km. The fault surface break cuts through the heavily degraded rim of an unnamed ~20-km-diameter impact crater. The structural relief of the landform appears unaffected by this crater. The surface break and shape of the landform both indicate that the fault system underlying Ogygis Rupes dips to the northwest and strikes NE–SW. A set of smaller thrust fault-related landforms accompanies Ogygis Rupes to the northwest. Those faults strike approximately parallel to Ogygis Rupes, and on the basis of their surface expressions, they have synthetic (i.e., northwest) and antithetic (i.e., southeast) dip directions.

Interestingly, a series of parallel river channels is superposed on the gentle backslope of the landform, most notably in its southern portion (Figure 3). The alignment of these channels, downslope on the Ogygis Rupes landform, attests to the presence and flow of liquid water during or after the structural relief was established and thus ties the fluvial processes shaping the channels to the tectonically controlled topography at this location. These fluvial landforms are not found to have modified the structural relief of Ogygis Rupes substantially.

The variations in structural relief from which we interpret the throw distribution profile for this fault show steep increases of ~75 m/km from the tips toward the center, except at and around the overlap region of the two fault segments, where the structural relief remains constant at around 800 m (Figure 3). The structural relief and thus presumably fault throws consistently exceed 1,000 m in the central part of the landform. The throw maximum of 2,152 m occurs about 80 km north of the southern fault tip, with another peak occurring ~20 km south of the northern fault tip, such that the throw distribution somewhat asymmetrical.

The observation of one fault segment terminating at the other, the large overlap-to-spacing ratio of >10, and the overall throw distribution together indicate that the two fault segments are hard linked (i.e., are physically connected), such that they serve to build the observed structural relief as one fault system. Furthermore, the throw distribution of Ogygis Rupes is typical for unrestricted fault growth (e.g., Nicol et al., 1996), with the observed map pattern and deviations from a perfectly peaked throw distribution likely arising from minor topographic modification and interaction and linkage of several smaller fault segments as they formed the larger array.

3.2. Bosphorus Rupes

Bosphorus Rupes is centered at 42.7°S, 57.6°W. It is a 542-km-long thrust fault-related landform situated near the northwestern rim of Argyre basin. Its map pattern indicates that this landform is composed of two major

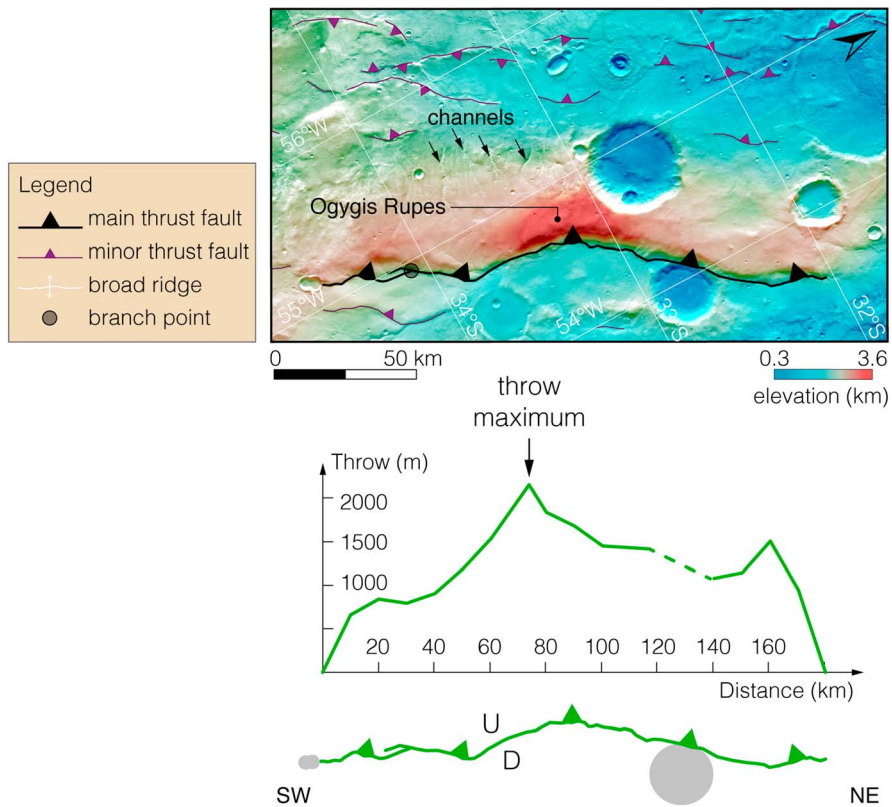


Figure 3. Map of fault traces (top) and throw distribution interpreted from structural relief measurements (bottom) of faults associated with Ogygis Rupes. Thrust faults associated with Ogygis Rupes are displayed on a THEMIS mosaic overlaid with MOLA topography in orthographic projection centered at 54.6°W, 33.1°S. The hanging wall and footwall are referenced on the map with their respective upward (U) and downward (D) movements relative to one another. Arrows on map indicate the location of fluvial channels. The gray circles represent impact structures. The map symbology used here applies to all subsequent maps.

fault segments. Segment 1 is the southernmost and is 308 km long; segment 2 lies to the north and has a length of 232 km (Figure 4). These two segments show 2 km of underlap. Both fault segments underlying Bosphorus Rupes dip to the northwest and strike NE–SW, similar in orientation to the nearby Ogygis Rupes (Figure 3). As with Ogygis Rupes, a few smaller thrust fault-related landforms accompany Bosphorus Rupes to the northwest, again oriented subparallel to the larger structure and again with both synthetic (northwest) and antithetic (southeast) dip directions. Additionally, segment 1 shows two larger fault splays toward its northern tip; segment 2 has one small splay at its northern tip (Figure 4).

Two craters, 30 km and 23 km in diameter, respectively, are superposed on the southern end of segment 2 (Figure 4). The fault-related topography has been partially removed by the bigger (northern) crater and entirely erased by the smaller of the two craters. Both are largely degraded, and thus, they are presumably very old (Robbins & Hynek, 2012). The stratigraphic relationship of the fault with these craters indicates that the faulting responsible for Bosphorus Rupes was active at the time of emplacement of the larger crater.

The structural relief from which the throw distribution for these fault segment profiles is interpreted shows moderate to steep increases of up to 30 m/km from the tips to the centers of the segments. Segment 1 shows pronounced variations in fault-related topography, with its throw maximum of 1,648 m located near the center of the landform (Figure 4), and another throw maximum above 1,500 m situated about 100 km from its southern tip. In addition, two local minima of less than 500 m of structural relief occur along the throw distribution. Segment 2 consistently shows throws above 1,200 m in its central portion, with a maximum of 1,737 m asymmetrically skewed toward the north (Figure 4).

Analogous to observations from Terran thrust fault displacement variations (Ellis & Dunlap, 1988), we interpret the observed variations in fault throw, as well as evidence for splays and jogs (i.e., sudden bends in

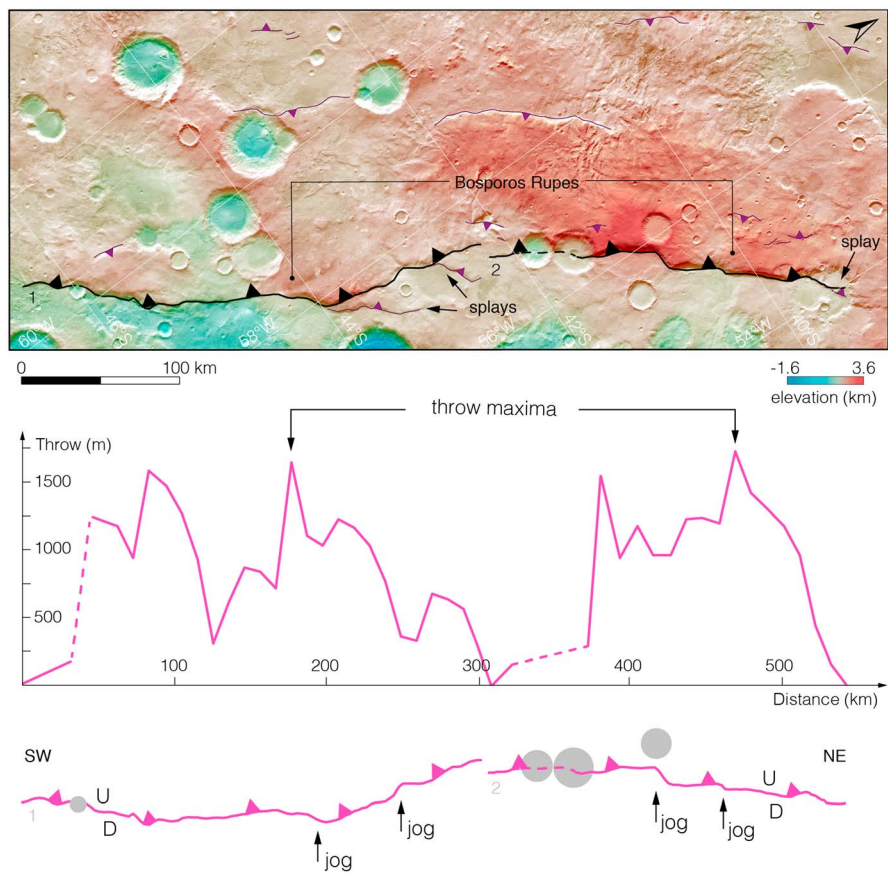


Figure 4. Map of fault traces (top) and throw distributions (bottom) of faults associated with Bosporos Rupes. Thrust faults associated with Bosporos Rupes are displayed on a THEMIS mosaic overlaid with MOLA topography in orthographic projection centered at 57.5°W, 42.5°S.

the fault surface break; Sibson, 1986) in the map pattern (Figure 4), as remnant artifacts of smaller individual segments that coalesced into the large structures that we observe today. The observed underlap between the two segments indicates that they are not linked and that they have not meaningfully interacted (i.e., shared or distributed displacement) with one another.

3.3. Phrixi Rupes

Phrixi Rupes, centered at 44.6°S, 67.1°W, is a 177-km-long thrust fault-related landform. Its map pattern indicates that this landform is formed by three major fault segments (Figure 5), with two forming fault system 1 and one segment forming fault 2. Fault system 1 has a total length of 145 km, and the two major fault segments of which it is composed show an underlap of less than 1 km, about 80 km from its southern tip. The underlap region, however, shows three minor fault scarps. Fault 2 is 65 km long (Table 1). Fault system 1 and fault 2 have an overlap of 33 km and a spacing of 10 to 15 km, which yields an overlap-to-spacing ratio of 2–3. Both fault systems underlying Phrixi Rupes dip to the northwest and strike NE–SW, following the regional trend established by Bosporos and Ogygis Rupes (Figures 3 and 4). No major impact structures crosscut the surface break of the fault, and only one 13-km-diameter crater superposes (and so modifies) the structural relief near the northern tip of fault 2.

The variations in structural relief that inform the fault throw distributions show clear peaks in both landforms (Figure 5). The throw maximum that we identified at 603 m for fault system 1 is somewhat skewed to the south, and another peak measured with a throw of ~550 m occurs farther to the north. A somewhat lower displacement is observed in the fault center. Despite this complexity, the overall shape of the throw distribution is symmetric (Figure 5). Fault 2 also has a generally symmetric throw profile, with a maximum of 1,421 m occurring at the center of the fault.

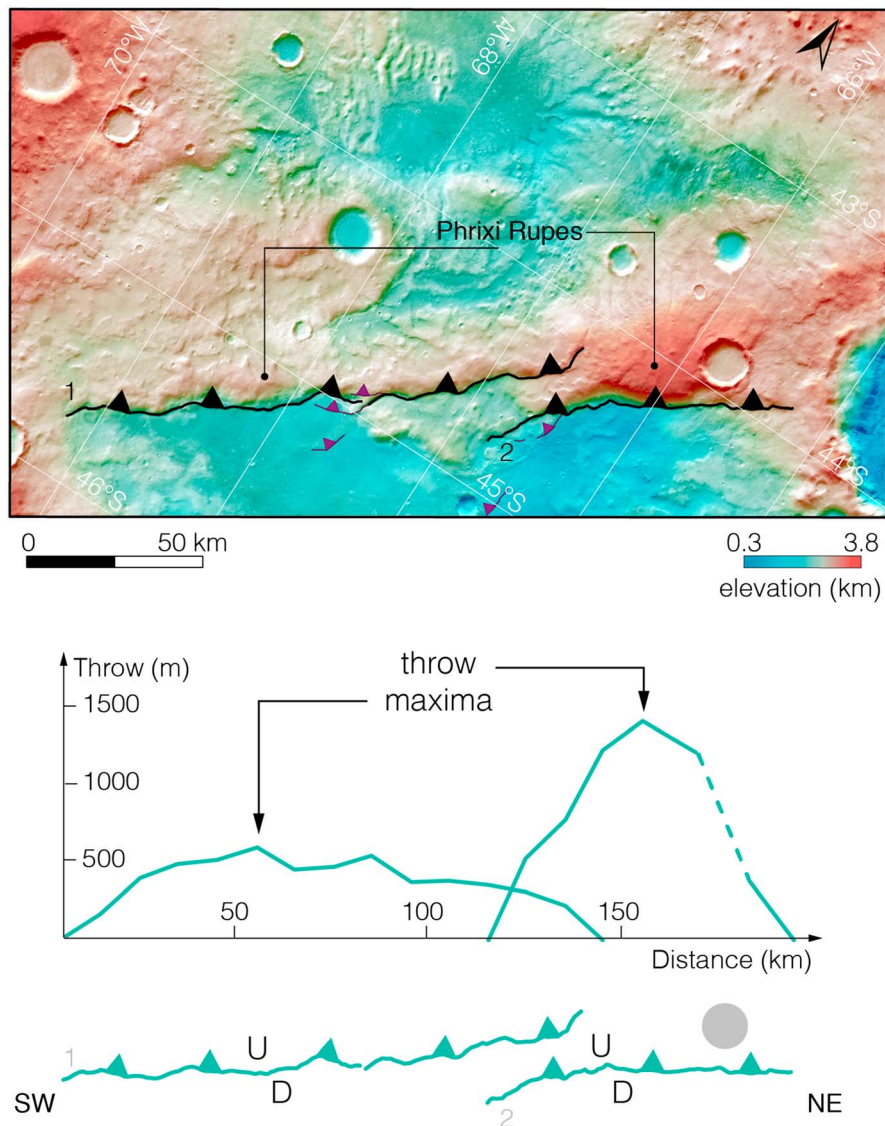


Figure 5. Map of fault traces (top) and throw distribution (bottom) of faults associated with Phrixi Rupes. Thrust faults associated with Phrixi Rupes are displayed on a THEMIS mosaic overlaid with MOLA topography in orthographic projection centered at 67.0°W , 44.6°S .

The two segments in fault system 1 are interpreted here to be linked, as evident from the continuous and symmetric throw distribution. The observed lower displacement between the two peaks within this fault system corresponds to the minor fault scarps and thus may represent a breached step over region between the two fault segments. The throw distribution for fault system 1 is less pronounced than that of fault 2, which we attribute to the coalescence and linkage of the two constituent segments. That the throw maxima for both profiles occur at or near the centers of their faults, rather than being obviously skewed toward the overlap region, may indicate that these two faults have not substantially interacted with one another. The peaked and symmetric shapes of the throw distribution profiles are consistent with unrestricted (i.e., uninhibited) fault growth. However, an overlap-to-spacing ratio of 2–3, as is observed for these structures, is commonly found for interacting faults on Earth (Willemse, 1997). Thus, we cannot rule out that these faults have exerted some influence on each other during their growth.

3.4. Icaria Rupes

Icaria Rupes is located at 35.8°S , 139.6°W , and has a length of 165 km. It consists of one major fault segment accompanied by a series of minor thrust faults (Figure 6). The surface break of the major structure curves

Table 1

Measured Lengths and Throw Maxima Interpreted From Structural Relief Measurements for Thrust Fault Segments of This Study, Including Inferred Maximum Displacements for a Fault Dip Angle of $30^\circ \pm 10^\circ$ and Notes on the Fault Map Patterns, Where Applicable

Landform	Figure	L (km)	t_{\max} (m)	D_{\max} (m)			Notes
				20°	30°	40°	
Ogygis Rupes	Figure 3	181	2,152	6292	4304	3348	
Bosporos Rupes 1	Figure 4	308	1,648	4818	3296	2564	
Bosporos Rupes 2		232	1,737	5079	3474	2702	2 km underlap
Phixi Rupes 1	Figure 5	145	603	1763	1206	938	
Phixi Rupes 2		65	1,421	4155	2842	2211	33 km overlap
Icaria Rupes	Figure 6	165	1,175	3435	2350	1828	
Hiddekel Rupes 1	Figure 7	167	445	1301	890	692	
Hiddekel Rupes 2		136	380	1111	760	591	10 km underlap
Dorsa Brevia 1	Figure 8	283	965	2821	1930	1501	
Dorsa Brevia 2		242	894	2614	1788	1391	50 km overlap
Thyles Rupes 1A	Figure 9	119	950	2778	1900	1478	59 km overlap between 1A and 1B;
Thyles Rupes 1B		269	1,700	4970	3400	2645	195 km overlap between 1B and 1C
Thyles Rupes 1C		264	1,110	3245	2220	1727	13 km underlap between 1A and 1C
Thyles Rupes 1A-C		394	2,450	7163	4900	3812	
Thyles Rupes 2	Figure 9	242	1,198	3503	2396	1864	
Thyles Rupes 3	Figure 9	217	1,722	5035	3444	2679	
Phlegra Montes 1	Figure 10	319	1,297	3792	2594	2018	74 km overlap between 1 and 2
Phlegra Montes 2		265	2,596	7590	5192	4039	Full overlap with 3
Phlegra Montes 3		262	2367	6921	4734	3682	
Phlegra Montes 4		400	2,692	7871	5384	4188	
Phlegra Montes 5		106	1,172	3427	2344	1823	Full overlap with 4
Phlegra Montes 4 & 5		400	3,375	9868	6750	5251	
Phlegra Montes 6		94	579	1693	1158	901	Full overlap with 7
Phlegra Montes 7		372	2,071	6056	4142	3222	
Phlegra Montes 8		446	647	1892	1294	1007	228 km overlap between 7 and 8
Phlegra Montes 9		69	593	1734	1186	923	Full overlap with 8
Phlegra Montes 7-9		590	2,071	6055	4142	3222	

Note. Values shown in bold are compiled from cumulative throw distributions.

around a 30-km-wide circular mensa, with the minor thrust faults occurring in the footwall of the major structure alongside that mensa. A prominent fault jog is observed toward the southern fault tip. Icaria Rupes strikes NW–SE, and the asymmetry of the landform indicates that its underlying fault system dips to the northeast. The surface break of this fault shows crosscutting relationships with two craters: a ~10-km-diameter crater superposes the fault near its northern tip, whereas two craters—a 35-km-diameter crater beneath a 13-km-diameter crater—are cut by the fault. The heavily degraded crater is consistent with an emplacement time during the Noachian (e.g., Craddock & Maxwell, 1993; Mangold et al., 2012), placing the fault activity during or after this time system.

The variations of structural relief show steep increases of up to 40 m/km from the tip toward the center. A relief of more than 1,000 m is found along the entire central part of the landform. The maximum structural relief that we interpret to correspond to the throw maximum is measured at 1,175 m and occurs somewhat closer to the northern fault tip, but the throw distribution profile is generally symmetric. The throw values are highest, and consistently around 1,000 m, along the entire region where the fault curves around the mensa.

We interpret the map pattern of this fault system as indicative of the horizontal displacement along this large structure being impeded at the center by the preexisting mensa, forming a ramp. The unobstructed portions of the fault form a bend in the map pattern of the shortening structure that is accompanied by small-scale fault-related folds at its leading edge (Figure 6). The highest throw values, which are consistently around 1,000 m along the entire region where the thrust fault is obstructed by the mensa, indicate that the location of this obstruction likely had a major influence on the growth of the landform, and may have restricted the fault growth.

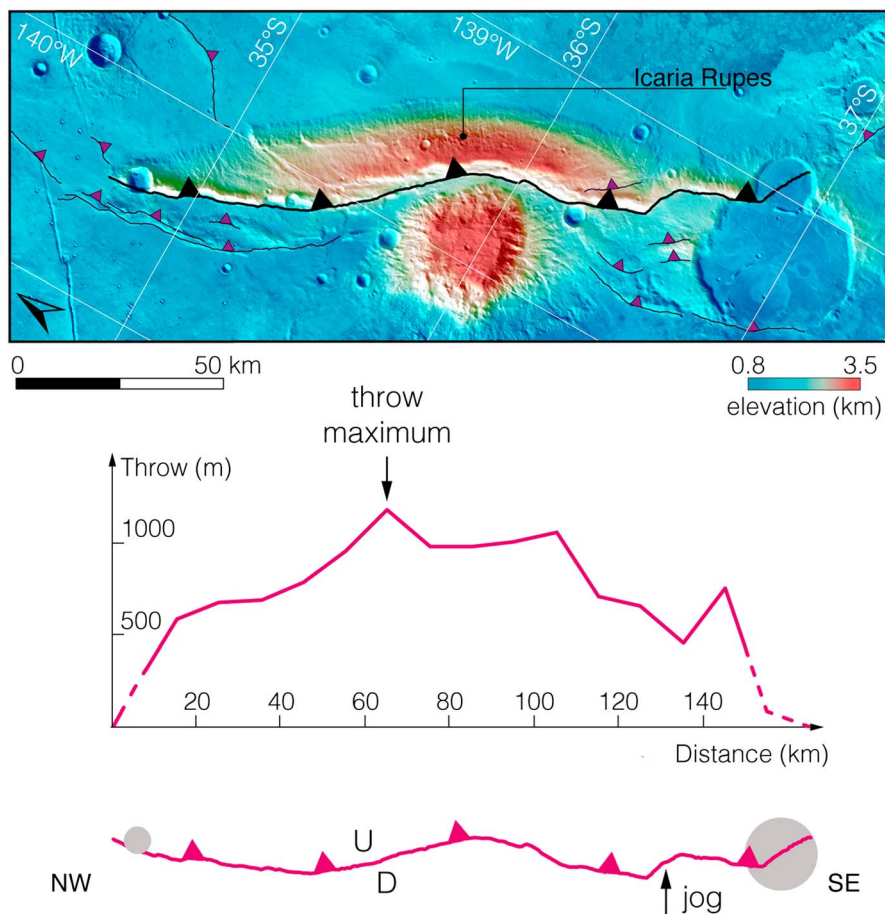


Figure 6. Map of fault traces (top) and throw distribution (bottom) of faults associated with Icaria Rupes. Thrust faults associated with Icaria Rupes are displayed on a THEMIS mosaic overlaid with MOLA topography in orthographic projection centered at 139.6°W, 35.9°S.

3.5. Hiddekel Rupes

Hiddekel Rupes, centered at 16.7°N, 16.5°E, consists of two thrust fault-related landforms that together sum to a total length of 313 km (Figure 7). Fault 1 has a minimum length of 167 km, dips to the southwest, and strikes NW–SE. The fault surface break of fault 1 shows a crosscutting relationship with a ~30-km-diameter crater, which partially erased the structural uplift. The surface break of fault 2 is 136 km long, which dips to the east—almost the diametric opposite of fault 1—and strikes approximately N–S. The two faults show an underlap of ~10 km. Within the underlap region, several minor thrust faults are present.

The topographic variations for Hiddekel Rupes show symmetric increases of structural relief from the tips toward the fault center for both faults (Figure 7). The maxima for fault-related topography are found to be 445 and 380 m for faults 1 and 2, respectively. Fault 1 shows a peaked profile shape with its throw maximum just north of the fault center. The fault has a throw minimum in the southern central portion of the fault (Figure 7), which occurs where the surface break shows a pronounced bend in map view. This site is also host to a small fluvial channel system that cuts through the crest of the landform, with fluid discharge likely having occurred toward the leading edge. Some of the structural relief may thus have been eroded, and the location of the channel may in turn be structurally controlled at this site. Fault 2 also has a peaked throw distribution profile, with its throw maximum somewhat skewed toward its northern tip.

We interpret the generally peaked shapes of both throw distribution profiles as consistent with largely unrestricted fault growth. The presence of minor thrust fault-related landforms in the underlap region is likely caused by some interaction between the faults beneath the two main landforms. As the faults dip in opposite directions, it is likely that such fault interaction did not substantively influence their throw distributions.

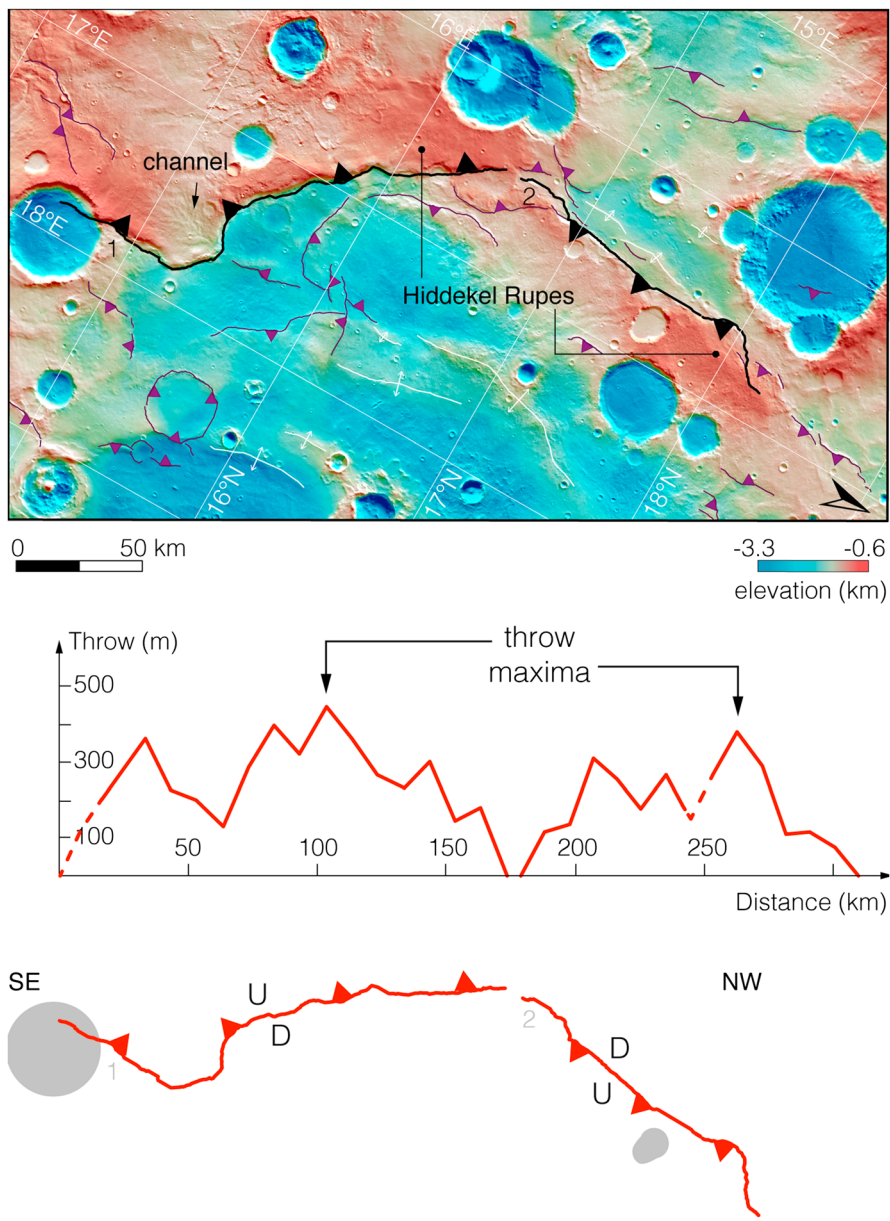


Figure 7. Map of fault traces (top) and throw distribution (bottom) of faults associated with Hiddekel Rupes. Thrust faults associated with Hiddekel Rupes are displayed on a THEMIS mosaic overlaid with MOLA topography in orthographic projection centered at 16.56°E; 16.5°N.

Hiddekel Rupes is located at the eastern edge of a heavily modified and volcanically filled ~410-km-diameter impact basin, and so it may be that this landform localized at the rim of the basin. Several other thrust fault-related landforms occur in the region inside that basin, which have no predominant regional trend but either loosely follow a basin-concentric pattern or form rings (Figure 7) that outline the rims of buried impact craters. Broad tectonic ridges with no clear fault surface break, similar to those mapped in Mare Crisium on the Moon (Byrne et al., 2015), are also present in the region (Figure 7).

3.6. Dorsa Brevia

Dorsa Brevia is a 651-km-long set of ridges consisting of at least four individual thrust fault-related landforms, centered at 71.1°S and 63.2°E. We mapped and analyzed two landforms at its westernmost extent (Figure 8). Both landforms have fault surface breaks that are curvilinear in map view, with fault strikes of WNW–ESE and

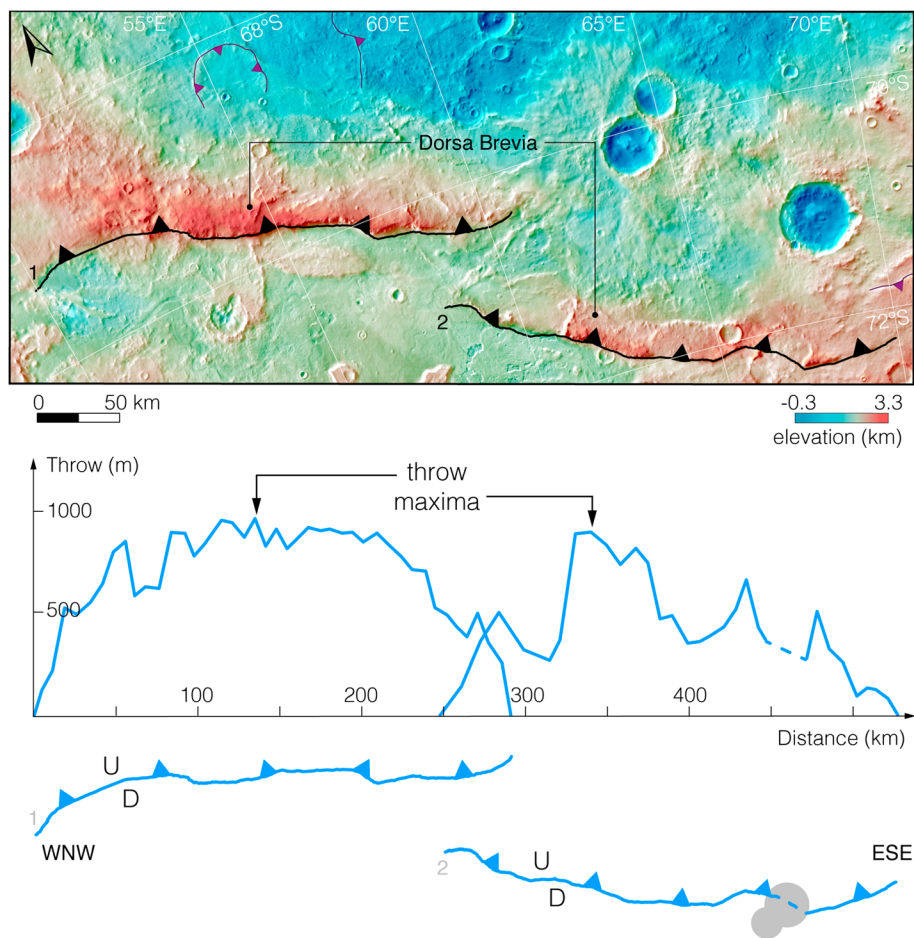


Figure 8. Map of fault traces (top) and throw distribution (bottom) of faults associated with Dorsa Brevia. Thrust faults associated with Dorsa Brevia are displayed on a THEMIS mosaic overlaid with MOLA topography in orthographic projection centered at 58.0°E, 71.0°S.

dips close to NNE. The fault surface break of fault 1 has a length of 283 km, whereas the surface break of fault 2 is 242 km long (Table 1). The two faults show an overlap of ~50 km with a horizontal spacing of 40 to 55 km, such that the overlap-to-spacing ratio is ~1. Fault 2 is spatially collocated with a heavily degraded impact crater toward its eastern tip. Although definitive crosscutting relations between the fault and the crater are unclear, the topographic expression of the fault is less prominent within the crater, and, thus, it is interpreted to have been erased. On the basis of the crater's degradation state, the fault activity that formed this landform must have occurred very early in the geological history of Mars.

The variations in topographic relief and thus throw distribution for fault 1 shows moderate to steep, symmetrical increases in throw of up to 30 m/km at the fault tips, and a flat-topped throw distribution toward the fault center, where the throw maximum of 965 m occurs (Figure 8). The profile for fault 2 shows moderate increases in fault-related topography of up to 10 m/km from the tips toward the center and has a generally peaked shape. The maximum throw of 894 m is skewed toward the WNW.

The overlap-to-spacing ratio of ~1, as well as the slight asymmetry in the throw distribution for fault 2 skewed toward fault 1, indicates that these two faults have interacted to some extent. The overlap region may be host to secondary structures that accommodated strain as part of the fault interaction, but a nearby ejecta blanket from a crater located at ~70°S, 64°E, superposes or modifies any small-scale landforms in the region. Furthermore, the flat-topped throw distribution profile shape of fault 1 indicates that it may have largely grown in an unrestricted manner, albeit with some horizontal restriction by a mechanical barrier at depth. The peaked throw distribution profile shape of fault 2 is consistent with unrestricted fault growth. Fault 2

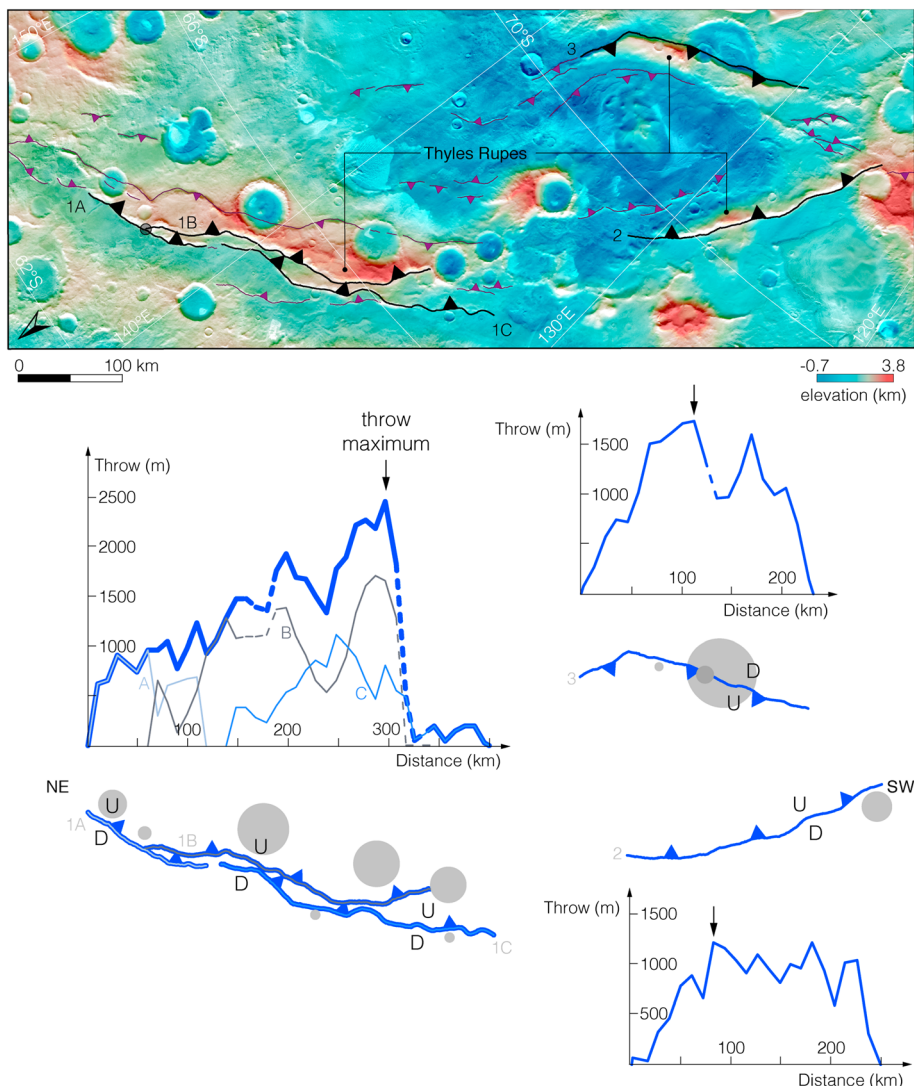


Figure 9. Map of fault traces (top) and throw distributions (bottom) of faults associated with Thyles Rupes. Thrust faults associated with Thyles Rupes are displayed on a THEMIS mosaic overlaid with MOLA topography in orthographic projection centered at 136.0°E, 70.0°S. Throw distributions shown in bold lines are cumulative throws.

shows a lower throw maximum compared with fault 1, which may indicate that the former is not large enough for the mechanical barrier to have influenced its fault throw distribution.

3.7. Thyles Rupes

Thyles Rupes, centered at 69.3°S, 132.3°E, consists of three major and multiple minor thrust fault-related landforms (Figure 9). There is a pronounced regional structural trend present here, as all landforms strike roughly NNE–SSW. The first thrust fault-related landform consists of three pronounced fault segments (segments 1A–C). Segment 1A is 119 km long, segment 1B has a length of 269 km, and segment 1C is 264 km long (Table 1). Segment 1A shows a 59 km overlap with segment 1B and 13 km underlap with segment 1C. Segments 1B and 1C have a remarkably large overlap of 195 km. Segment 1B terminates near the center of segment 1A, forming a branch point. The fault planes dip to the ESE and are very closely spaced, with spacing values as small as 5 km. These three main fault segments are accompanied by an array of small, antithetically dipping faults that likely acted as back thrusts. Additionally, a few small thrust fault-related landforms with faults dipping synthetically to the main fault array are present in the footwall of the thrust system.

The second major landform (Fault 2) that constitutes Thyles Rupes is a single fault 242 km long. It strikes NE-SW and dips to the southeast (Figure 9). The third landform (Fault 3) shows a single, 217-km-long fault surface break that strikes NE-SW and dips to the northwest. The hanging walls of Thyles Rupes faults 2 and 3 are both accompanied by a series of minor thrust fault-related landforms that have their underlying faults dipping synthetically to the major faults with which they are associated.

All landforms show crosscutting relationships with heavily degraded craters, but no impact structure has substantively erased the structural relief produced by the faults. Interestingly, fault 3 cuts through a 70-km-diameter, moderately degraded crater that appears to have an elliptical shape and thus may have been shortened (Egea-González et al., 2017). The long axis of the crater is parallel to the fault strike and is 10 km longer than the short axis (Figure 9). Within the large crater, the fault is superposed by another ~15-km-diameter crater. The two craters possess the same morphological degradation state (Robbins & Hynek, 2012), which places the fault activity within the narrow time window between the emplacements of these two craters. Crater statistics across this landform produce a model age for fault 3 of ~3.8 Ga (Egea-González et al., 2017).

All individual variations in structural relief and therefore throw distribution profiles show moderate to steep increases in structural relief of up to 20 m/km from their respective fault tips toward their centers. Fault segment 1A has a symmetric throw distribution profile with a throw maximum of 950 m. Fault segment 1B has a throw maximum of 1,700 m skewed to its southern tip, whereas fault segment 1C has a peaked profile with a throw maximum of 1,110 m occurring exactly where segment 1B has a local minimum (Figure 9). The throw distribution profile for fault 2 shows steep and generally symmetrical increases in throw from the fault tips, and a flat-topped throw distribution toward the fault center. The throw maximum of 1,198 m occurs toward the northern fault tip (Figure 9). The profile for fault 3 shows steep increases in throw from the tips toward the center and has a generally peaked shape. The throw maximum of 1,722 m occurs near the fault center.

The throw distribution profile shapes for Thyles Rupes 2 and 3 are interpreted here as consistent with unrestricted fault growth, but some horizontal restriction because of a mechanical barrier at depth accounts for the flat-topped throw distribution of fault 2. The large overlaps, narrow spacing, and shared orientations of the fault surface breaks of fault segments 1A to C suggest that they acted as one fault system to build the structural relief, such that their individual throw distributions are likely more representative of the fault system when they are interpreted as representing a cumulative (*i.e.*, summed) throw distribution. The cumulative throw distribution profile has a pronounced asymmetric shape, and a nearly linear throw gradient of ~6 m/km persists for most of the length of the fault system. The throw maximum of 2,450 m is skewed markedly toward its southern tip (Figure 9), where it drops off very steeply at nearly 100 m/km.

3.8. Phlegra Montes

The Phlegra Montes are an elongate, topographically elevated set of landforms more than 1,400 km long, centered at 40.4°N and 163.7°E and composed of nine major and several minor thrust fault-related structures (Figure 10). The many knobs in the region that give the Phlegra Montes their name are generally more pronounced on the hanging wall side of the large thrust faults present. All thrust faults in this region strike N-S and dip either to the east (segments 1, 3, and 6) or west (segments 2, 4, 5, and 7–9). The fault segments range in length from 69 to 400 km and display various amounts of overlap with one another (Table 1).

The Phlegra Montes are spatially associated with many craters (van Gasselt et al., 2015), at least some of which may have modified or removed portions of the structural relief (Figure 10). Only two craters are observed to directly superpose the surface breaks of the thrust faults at segments 4 and 8, respectively (Figure 10). Furthermore, the 95-km-diameter Adams crater, the largest crater in the region, lies just to the south of the southern tips of fault segments 2 and 3. Adams crater is not crosscut by these faults, although its ejecta blanket is, which indicates that some fault activity postdates the emplacement crater. Crater areal density measurements indicate that the Phlegra Montes have been affected by an order-of-magnitude greater denudation rate compared with the average rate for Mars (van Gasselt et al., 2015), and so the preserved structural relief may represent only the minimum vertical displacement on the thrust faults in this region.

The distributions in structural relief of the individual landforms for faults 1–4 and 7–9, which we take here to correspond closely to their throw distributions, show pronounced asymmetries, with throw maxima skewed toward the neighboring faults. Faults 5 and 6, which are among the shortest faults in this fault

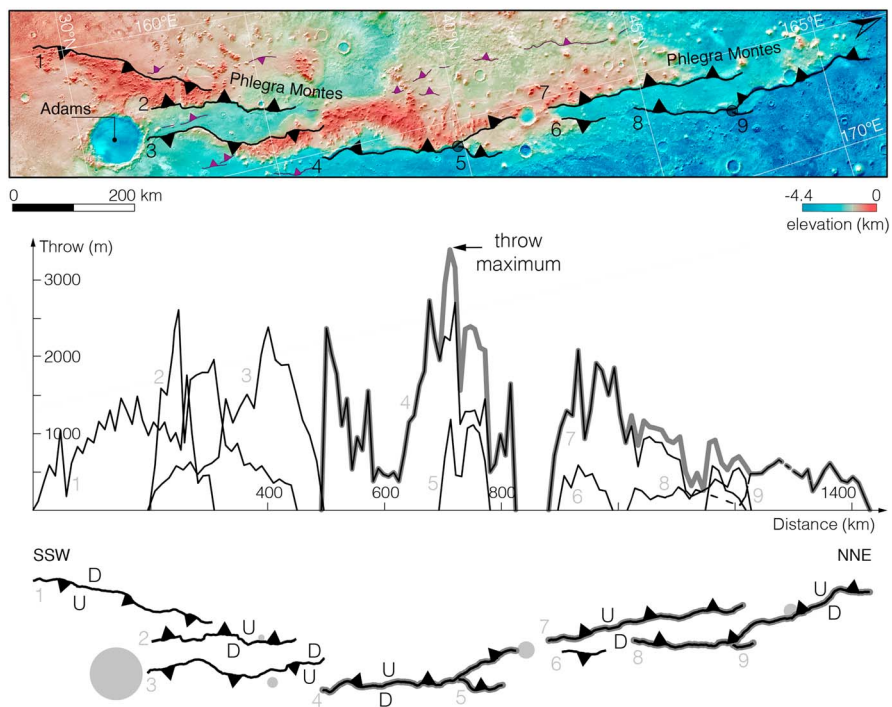


Figure 10. Map of fault traces (top) and throw distribution (bottom) of faults associated with the Phlegra Montes. Thrust faults at the Phlegra Montes are displayed on a THEMIS mosaic overlaid with MOLA topography in orthographic projection centered at 165°E, 40.5°N. Throw distributions shown in bold lines are cumulative throws.

array, have generally symmetric throw distribution profiles. Individual throw maxima range from 579 m for the 94-km-long fault 6 to as much as 2,692 m for the 446-km-long fault 8 (Table 1). In particular, the 319-km-long fault 1 overlaps with the 165-km-long fault 2 by 74 km. Within this overlap region, both faults show their maximum throws of 1,297 and 2,596 m, respectively. Fault 2 also entirely overlaps fault 3, which is 262 km long. Faults 3 and 4 show minimal overlap but the maximum of 2,367 m of the throw distribution of fault 3 is skewed toward fault segment 4. The throw distribution of the 400-km-long fault segment 4 shows steep increases in throw at the fault tips and has multiple maxima and minima (Figure 10), with the highest throw values of 2,692 m near its overlap with fault segment 5. Segment 5, a structure 106 km long, overlaps entirely with fault segment 4 and shows a symmetric and peaked throw distribution with the throw maximum measured at 1,172 m. The map pattern shows that the southern tip of fault segment 5 terminates at fault 4, forming a branch point. Segment 6 is 94 km long and has a peaked, symmetrical throw distribution with a maximum of 579 m. Segment 7, which entirely overlaps segments 6, is 372 km long and has a pronounced asymmetric throw distribution with a maximum of 2,071 m skewed toward fault 4 to the south. The 446-km-long fault segment 8 overlaps with segment 7 by 228 km and shows an asymmetric throw distribution with a maximum of 647 m skewed to the north. Faults 7 and 8 have a spacing of ~45 km, yielding an overlap-to-spacing ratio of ~5. Fault segment 9 is 69 km long and its southern tip terminates at segment 8, forming another branch point. The throw distribution of segment 9 is symmetric, with a maximum of 593 m.

Because of their very similar strikes and dips, and their map patterns indicating large overlaps or terminations of structures in one another, we interpret segments 4 and 5, as well as 7–9, to have built the structural relief associated with the landforms they underlie as a single fault system, and so their throw distribution profiles are shown as cumulative in Figure 10. The cumulative throw distribution for faults 4 and 5 shows two maxima and a minimum dropping below 500 m near the central portion of the fault (Figure 10). The throw maximum in the southern portion of the fault array, measured at 2,357 m, is both similar to and skewed toward fault segment 3. The throw distribution profile for faults 4 and 5 shows its second maximum of 3,375 m—the largest throw measured for this fault system—near the center of the fault array. The cumulative throw

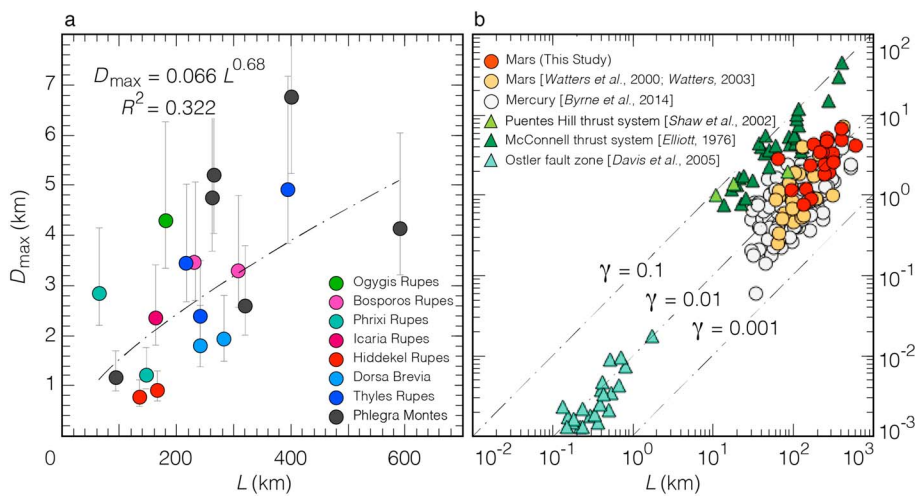


Figure 11. Inferred maximum displacements of thrust faults as a function of map lengths. (a) Scatter plot of thrust fault data acquired in this study with a best fit power law. (b) Subset of D_{\max}/L scaling compilation of Klimczak et al. (2010) only showing thrust faults. Data sets for thrust faults on Mars (this study; Watters et al., 2000; Watters, 2003b) (red/orange symbols) and Mercury (Byrne et al., 2014) (gray symbols) shown for comparison to Terran faults (green symbols). The dashed curves indicate linear scaling functions (equation (1)) with γ values of 10^{-1} , 10^{-2} , and 10^{-3} . Displacements for Terran thrust faults represent the measured true displacements; displacements for thrust faults on Mars and Mercury are plotted for assumed dip angles of 30° with $\pm 10^\circ$ uncertainty shown in (a).

distribution profile for fault segments 7–9, dominated by and thus very similar to fault 7, is asymmetrical, with the throw maximum of 2,071 m skewed toward fault segment 4.

The pronounced asymmetries of the faults with throw maxima skewed toward neighboring structures indicate that substantial fault interaction took place at the Phlegra Montes. The overall throw distribution profile for the entire segmented fault system at the Phlegra Montes shows steep increases in throw from the fault system ends, and a peaked shape with linear displacement gradients on either side of the throw maximum (Figure 10). These characteristics indicate that the individual fault segments likely grew as a single, large fault system that deeply penetrates the Martian lithosphere, likely growing in an unrestricted manner.

4. Fault Scaling

We analyzed the map pattern and topographic expressions of eight thrust fault systems on Mars, composed of 19 thrust fault-related landforms with a total of 24 fault segments, to derive throw distributions and identify the throw maxima. From the maximum throw values and assumptions of fault dip angles (see section 2), the maximum displacements of the thrust faults can be estimated. The resultant maximum displacements and their corresponding lengths (Table 1) were then paired to derive the maximum displacement-to-length (D_{\max}/L) statistic.

The D_{\max}/L statistic shows a large scatter in the data ranging from 65- to 590-km-long faults and fault arrays, with maximum displacements from as low as 760 m to as much as 6750 m (Figure 11a and Table 1). Following the regression approach for fault scaling relationships by Clark and Cox (1996), we computed the best fit power law for the investigated thrust faults. Results return a scaling coefficient of $\gamma = 0.066$ and an exponent of $c = 0.68$ (Figure 11a), with a poor goodness of fit indicated by a coefficient of determination of $R^2 = 0.322$.

The poor fit may arise from both geologic processes involved in faulting and the methods by which the measurements are made (see discussion in Cowie & Scholz, 1992b), but it is not uncommon for fault populations to display a scatter in the data that spans over almost an order of magnitude (e.g., Cartwright et al., 1995; Schlische et al., 1996). The analyzed thrust faults on Mars may have grown as part of multiple different thrust fault populations, and so the structures may not all have accommodated strain with the same structural style or the same dips as assumed here. Furthermore, interactions among faults, as well as variations in physical

properties encountered by the faults during growth, may have contributed to the data scatter. This scatter may further reflect fault growth being influenced by regional variations in rock-mechanical properties of the lithosphere (e.g., Peacock, 1991), faults being in different stages of the fault linkage process (e.g., Cartwright et al., 1995), faults having maximum displacements not representative of the overall displacement of the fault or maximum displacements occurring at different depths on the fault plane (Cowie & Scholz, 1992b), the restriction of fault growth due to stress perturbations/transfer at the fault tips (Nicol et al., 1996), or mechanical barriers in the lithosphere inhibiting fault growth (e.g., Manighetti et al., 2001). Although we identified individual cases of restricted fault growth (for Icaria and Thyles Rupēs) and fault interaction (for Phlegra Montes), no single reason listed above can be identified here as the sole cause of the data scatter. Instead, we consider it likely that a combination of these reasons contributes to the large scatter of the data.

Under the assumption that our analysis sampled faults that are part of multiple populations, then different regional tectonic processes must have produced stresses favorable for thrust faulting across Mars. Nevertheless, individual faults within the same fault array and arguably as part of the same population—such as those observed at the Phlegra Montes, Bosphorus Rupes, and perhaps most strikingly observed at Phrixi Rupes (Figure 11a)—show a pronounced variability in displacement distribution shapes among themselves. This finding demonstrates that multiple regional thrust fault populations need not be invoked to explain the data scatter, but rather that fault growth on Mars is a complex process subject to numerous controlling factors, which is hardly surprising given the level of such complexity found for thrust fault growth and architecture on Earth (e.g., Boyer & Elliott, 1982; McClay, 1992).

The thrust faults evaluated in this study have scatter and a scaling coefficient comparable to those derived for two regionally confined populations of thrust fault-related landforms near the Martian dichotomy boundary (Figure 11b; Watters, 2003b; Watters et al., 2000), indicating that the scaling statistics derived here are representative of both global and regional scales on Mars. In addition, the scatter and scaling coefficient of thrust faults in this study are also similar to those derived from the population of thrust faults attributed to global contraction of Mercury (Figure 11b; Byrne et al., 2014). Although these arguments support the possibility that the thrust faults in this study belong to a single population, the D_{\max}/L statistics we derive are alone likely not sufficient to discriminate between a single and multiple fault population(s). The combined D_{\max}/L statistics across 12 different data sets of Terran faults, including normal, strike-slip, and thrust faults, show a near-linear scaling with a scaling ratio of $\gamma = 0.03$ (Schlische et al., 1996). This indicates that additional fault population statistics, such as size–frequency data, fault spacing, and overlap-to-spacing ratios across different regions on Mars would provide further information with which to distinguish between different fault populations.

The overlap of D_{\max}/L statistics between the thrust faults of this study, those recorded for thrust faults at the Martian dichotomy boundary (Watters, 2003b; Watters et al., 2000), and that measured for thrust faults on Mercury (Byrne et al., 2014) are likely due to the similarities of the planets on which they formed. Both Mercury and Mars are terrestrial planets with bulk basaltic lithospheres that have nearly the same surface gravitational accelerations, and this parameter in particular has been hypothesized to have had a major effect on the D_{\max}/L ratios of faults (Schultz et al., 2006).

Due to the structural complexity of many thrust systems, scaling relationships and displacement distributions are difficult to obtain and so fault scaling studies tend to focus on normal faults. However, a handful of studies exist for thrust fault scaling relationships (Davis et al., 2005; Elliott, 1976; Shaw et al., 2002; Figure 11b) and displacement distributions (Bi et al., 2018; Ellis & Dunlap, 1988) for Earth. Elliott (1976) realized that a relationship between fault displacement and length existed when studying the energy balance associated with the emplacement of the McConnell thrust sheet in the Canadian Rocky Mountains. Thrust faults there have similar range in fault length (13.5 to 410 km), but with much higher maximum displacements, than those we analyzed on Mars (Figure 11b). This difference may arise from the contrast in structural style of faulting (see discussion), and thus, the McConnell thrust sheet may not be the best Terran analogue to the thrust faults we observe on Mars. Three segments identified in the Puente Hills blind thrust fault system in California (Shaw et al., 2002) show similar D_{\max}/L ratios as those for the McConnell thrust sheet. Thrust faults of the Ostler fault zone in New Zealand that deform poorly consolidated Cenozoic sediments (Davis et al., 2005) show a range in lengths and displacements that is 2 orders of magnitude lower than for faults on Mars and Mercury, yet have similar D_{\max}/L ratios to structures on those two worlds.

5. Discussion

The thrust fault-related landforms on Mars analyzed in this study possess remarkable structural relief. The Martian mountain ranges generally involve a single or a few segmented major thrust faults and a series of accompanying minor thrust faults. Apart from the Phlegra Montes, these structures are usually found as isolated landforms that do not show any arrangements in long continuous mountain belts with multiple aligned and parallel landforms. The isolated structures show lengths of ~150 to ~400 km with relief of 1,000 to 2,500 m, but the Phlegra Montes reach a length of up to 1,400 km and boast relief of as much as 3,400 m. All topographic signatures were found to be asymmetric ridges, with a surface break at the base of the steep-sloped cliff. The lengths and amounts of uplift found for these landforms show that substantial mountain building took place on Mars and, given the widespread geographic distribution of these landforms across the planet (Figure 2), that it occurred on a global scale.

Mountain building on Earth is, either directly or indirectly, related to plate tectonics. Whether some primitive form of plate tectonics occurred on Mars is debated (e.g., Yin, 2012; also see detailed discussion in Barlow, 2008, p. 48–50), but there is no evidence for globally distributed, Earth-style plate tectonics preserved in its geologic record (e.g., Zuber, 2001). Mountain building on Mars, if related to some form of plate tectonics, would likely involve structural styles of faulting comparable to thrust belts on Earth, including multiple, long, sinuous thrust fault traces and complex landform morphology. The lack of such evidence further supports the view that Earth-style plate tectonics and associated formation of thrust-belt-style faulting did not prevail on Mars. Instead, the simple map patterns and landform morphologies favor structural styles commonly displayed by basement faults in intraplate settings.

Thus, tectonic processes found on one-plate planets, such as global contraction from planetary cooling (e.g., Andrews-Hanna et al., 2008; Mangold et al., 2000), lithospheric flexure (Watters, 2003b), and local or regional loading (Andrews-Hanna et al., 2008; Hauck et al., 2003), could be responsible for the planet's major thrust faults. Among these processes, global contraction may have had the potential to produce a global population of thrust faults (Solomon & Chaiken, 1976). Although the D_{\max}/L statistics do not allow us to unequivocally discriminate if the thrust faults investigated in this study are part of one global population, their widespread distribution (Figure 2), their broad range in orientations (Figures 3–10), their map patterns showing isolated landforms formed by one major structure and a series of accompanying minor thrust faults, and their substantial structural relief are not inconsistent with an origin from global contraction, and compare well with thrust faults attributed to global contraction on Mercury (Byrne et al., 2014). To further discriminate whether global contraction caused these structures to form, additional mapping and fault population statistics, as well as assessments of timing and rate of thrust faulting, are needed.

Given that large-scale thrust faults on Mars are thought to be able to penetrate to depths of ≥ 30 km (Egea-González et al., 2017; Grott et al., 2007; Schultz & Watters, 2001), or to as much as 48 km for Amenthes Rupes (Mueller et al., 2014), and based on the relatively simple map patterns and asymmetric cross-sectional topography of landforms in our study areas, the structural style of the thrust faulting analyzed here is comparable to Terran intraplate, basement-block faulting, and associated fault-propagation folding (i.e., fault-related anticlinal flexures of the rock volume in the hanging wall of the fault; e.g., Suppe & Medwedeff, 1990). Martian thrust faulting may also have involved the formation of extensive fault damage zones (Kim et al., 2004), shallowing of the dip angle with depth with the fault rooting into a deep basal décollement (e.g., Mueller et al., 2014), as well as ductile deformation and fabric development (Cowie et al., 2013) in lower lithospheric levels. Earth-analogue tectonic settings for this style of thrust faulting include the basement uplifts of the Laramide orogeny in the western United States (e.g., Erslev, 1986; Matthews, 1978; Stone, 1993) or the Late Cretaceous, intraplate, thrust-related basement uplifts and inversion tectonics of central Europe (the so-called *Saxonische Schollentektonik* or Saxonian block tectonics; e.g., Kley & Voigt, 2008; Ziegler et al., 1995). These uplifts are characterized by accommodation of strain predominantly along major thrust faults that are accompanied by fault-related folding, with relatively little strain being accommodated away from the major structures. Individual mountain ranges that may structurally compare well with the landforms observed on Mars thus include the Wind River Range in central Wyoming, as suggested by Mueller et al. (2014), and nearby mountain ranges such as the Beartooth or Bighorn Mountains, the East Kaibab Monocline (Byrne et al., 2016), or the Harz Mountains in Germany (e.g., Franzke et al., 2004; König & Wrede, 1994; Stackebrandt, 1983).

One of the principal findings of this study is that fault systems on Mars show substantial variation of their along-strike relief. The subsurface architectures of these structures therefore clearly cannot be modeled accurately with a single topographic profile. Throw distributions, in particular, indicate the locations of throw maxima along the faults, the presence or absence of fault growth restrictions, and interactions and linkage between fault segments. These parameters should inform future modeling efforts to better characterize the orientation and depth extent of the fault surface in the lithosphere.

This finding is illustrated best with our results for the Thyles Rupes thrust system. Forward mechanical modeling of fault-related surface displacements that were matched to observed topographic profiles in one location across Thyles Rupes 3 (Egea-González et al., 2017) indicates that the subsurface architecture of the thrust fault is likely characterized by a dip angle between 33° and 40° , a fault penetration depth of 15 to 20 km, and a fault slip of 1,900 to 2,100 m, whereas our analysis shows that maximum fault slips for these dip angles could be as high as \sim 2,680 to 3,160 m elsewhere on the fault. Derivations of local heat flow—made under the assumption that the penetration depth of the faults coincides with the brittle–ductile transition—are thus unreliable, because the topographic profile to which model solutions were fit was not positioned at the throw maximum and so the results for penetration depth and fault slip are not representative of the maximum possible values for this fault. In addition, the Thyles Rupes 3 fault displays a peaked throw distribution, which we interpret to correspond to unrestricted fault growth. This finding indicates that the fault has likely not penetrated the lithosphere deep enough to have encountered any major changes in mechanical properties of the lithosphere, especially not those associated with the brittle–ductile transition.

Furthermore, Thyles Rupes 1 shows distinct similarities in its cumulative throw distribution to displacement profiles of the Gladstone thrust fault array in New Zealand (Davis et al., 2005) and to a set of normal fault displacement distributions in the Afar region, East Africa (Manighetti et al., 2001). The systematic fault displacement gradient of the Gladstone thrust fault array was taken to be evidence that the individual fault segments link in the subsurface to a single slip surface (Davis et al., 2005), and this may be the case for the faults associated with Thyles Rupes. The strongly asymmetric shape of the displacement profiles in the Afar region was interpreted as the result of barriers to propagation at one fault tip and uninhibited fault propagation at the other (Manighetti et al., 2001). Although barriers such as changes in material strength from lithology or fracture density, or changes in local stress conditions from fault interaction (Manighetti et al., 2001; Nicol et al., 1996), are likely to have been present during major thrust faulting on Mars, it is unclear to what extent such changes caused fault tip restriction on the observed scale of Thyles Rupes 1. Nevertheless, the similarities of along-strike displacement distributions between Terran and Martian faults indicate that the mechanics of large thrust systems on Mars can be assessed by their variations in structural relief in a manner similar to those on Earth, despite uncertainties in subsurface architecture and kinematics.

6. Conclusions

The structural mapping and analysis of the variations in relief of 24 large thrust fault-related landforms on Mars show that these structures commonly have lengths of \sim 150 to \sim 400 km with uplifts of 1,000 to 2,500 m, although some examples can extend over 1,400 km in length with uplifts of as much as 3,400 m. The thrust faults underlying these landforms show a wide variety of map patterns and systematic along-strike variations in fault-related topography, which together enable the characterization of distributions in their vertical displacement component. The systematic along-strike relief variations of thrust faults on Mars, together with their similarity to displacement distributions of faults on Earth, confirms that to first order the mechanics of large thrust systems on Mars can be assessed by their variations in structural relief. The large thrust faults on Mars studied here display characteristics in their shape indicative of local differences in fault growth behavior, including unrestricted and restricted fault growth and substantial fault interaction and fault linkage. Implications arising from fault growth, interaction, and linkage highlight that future analyses of Martian lithospheric structure and rheology, heat flow, and seismicity using fault-related landforms must better account for such displacement variations along the fault by detailed analysis of their along-strike distributions.

We observe a wide diversity in thrust fault displacement distribution shapes, which is also reflected in the large scatter in the displacement-to-length scaling ratio. This finding is not surprising, given the widespread distribution of analyzed structures across the planet. This diversity is likely caused by a combination of factors including regional variations in rock properties and lithospheric structure, as well as differences in fault

growth geometries. Nevertheless, the widespread distribution of structures across Mars, their broad range in orientations, the generally simple, linear map patterns with only one or a few segments as part of a single major structure, their isolated occurrence, and their simple asymmetric cross-sectional topography are atypical for Earth-like plate-tectonic-style thrust belts such as the Himalaya or Alps. Instead, the Martian structures likely correspond to a style of faulting similar to that of intraplate basement-block faulting and associated fault-propagation folding on Earth, such as associated with the Laramide orogeny in the western United States or the late-Cretaceous block and inversion tectonics in central Europe.

Acknowledgments

C. K. and P. K. B. jointly planned this research; C. L. K. and C. K. carried out the mapping and collected the measurements. All of the authors contributed to interpretation and analysis of the data. C. K. and C. L. K. drafted the manuscript, and C. K. prepared the figures. We thank the IAU Working Group for Planetary System Nomenclature for approving the names for Icaria, Hiddekel, and Phixi Rupēs, which were previously unnamed. We also thank An Yin, Nancye Dawers, and Amanda Nahm for their thorough assessments of this research, which greatly improved this paper. This research was supported by the NASA Mars Data Analysis Program under grant NNX14AR89G. The methods and data used to produce the results of this paper are freely available in the published literature and via the NASA Planetary Data System.

References

- Anderson, E. M. (1942). *The dynamics of faulting and dyke formation with applications to Britain* (p. 191). Edinburgh, UK: Oliver and Boyd.
- Andrews-Hanna, J. C., Zuber, M. T., & Hauck, S. A. II (2008). Strike-slip faults on Mars: Observations and implications for global tectonics and geodynamics. *Journal of Geophysical Research*, 113, E08002. <https://doi.org/10.1029/2007JE002980>
- Apotria, T., & Wilkerson, M. S. (2002). Seismic expression and kinematics of a fault-related fold termination: Rosario structure, Maracaibo Basin, Venezuela. *Journal of Structural Geology*, 24(4), 671–687. [https://doi.org/10.1016/S0191-8141\(01\)00123-7](https://doi.org/10.1016/S0191-8141(01)00123-7)
- Barlow, N. (2008). *Mars: An introduction to its interior, surface and atmosphere* (p. 264). Cambridge, New York: Cambridge University Press. <https://doi.org/10.1017/CBO9780511536069>
- Bi, H., Zheng, W., Ge, W., Zhang, J. Z., & Yu, J. (2018). Constraining the distribution of vertical slip on the South Heli Shan Fault (northeastern Tibet) from high-resolution topographic data. *Journal of Geophysical Research: Solid Earth*, 123, 2484–2501. <https://doi.org/10.1002/2017JB014901>
- Boyer, S. E., & Elliott, D. (1982). Thrust systems. *American Association of Petroleum Geologists Bulletin*, 66, 1196–1203.
- Burgess, W. P., Yin, A., Dubey, C. S., Shen, Z.-K., & Kelty, T. K. (2012). Holocene shortening across the main frontal thrust zone in the eastern Himalaya. *Earth and Planetary Science Letters*, 357–358, 152–167.
- Byrne, P. K., Klimczak, C., & LaFond, J. K. (2016). The East Kaibab monocline: A Terran lobate scarp? *Lunar Planet. Sci. Conf.*, XLVII, Abstract 1022.
- Byrne, P. K., Klimczak, C., McGovern, P. J., Mazarico, E., James, P. B., Neumann, G. A., et al. (2015). Deep-seated thrust faults bound the Mare Crisium lunar mascon. *Earth and Planetary Science Letters*, 427(C), 183–190. <https://doi.org/10.1016/j.epsl.2015.06.022>
- Byrne, P. K., Klimczak, C., Şengör, A. M. C., Solomon, S. C., Watters, T. R., & Hauck, S. A. II (2014). Mercury's global contraction much greater than earlier estimates. *Nature Geoscience*, 7(4), 301–307. <https://doi.org/10.1038/ngeo2097>
- Caine, J. S., Evans, J. P., & Forster, C. B. (1996). Fault zone architecture and permeability structure. *Geology*, 24(11), 1025–1028. [https://doi.org/10.1130/0091-7613\(1996\)024%3C1025:FZAPS%3E2.3.CO;2](https://doi.org/10.1130/0091-7613(1996)024%3C1025:FZAPS%3E2.3.CO;2)
- Cartwright, J. A., Trudgill, B. D., & Mansfield, C. S. (1995). Fault growth by segment linkage: An explanation for scatter in maximum displacement and trace length data from the Canyonlands grabens of SE Utah. *Journal of Structural Geology*, 17(9), 1319–1326. [https://doi.org/10.1016/0191-8141\(95\)00033-A](https://doi.org/10.1016/0191-8141(95)00033-A)
- Chiarro, A. F., Schultz, P. H., & Masson, P. (1985). Global and regional ridge patterns on Mars. *Icarus*, 63(1), 153–174. [https://doi.org/10.1016/0019-1035\(85\)90025-9](https://doi.org/10.1016/0019-1035(85)90025-9)
- Clark, R. M., & Cox, S. (1996). A modern regression approach to determining fault displacement-length scaling relationships. *Journal of Structural Geology*, 18(2–3), 147–152. [https://doi.org/10.1016/S0191-8141\(96\)80040-X](https://doi.org/10.1016/S0191-8141(96)80040-X)
- Cowie, P. A., Scholz, C. H., Roberts, G. P., Faure Walker, J. P., & Steer, P. (2013). Viscous roots of active seismogenic faults revealed by geologic slip rate variations. *Nature Geoscience*, 6(12), 1036–1040. <https://doi.org/10.1038/ngeo1991>
- Cowie, P. A., & Scholz, C. H. (1992a). Physical explanation for the displacement-length relationship of faults using a post-yield fracture mechanics model. *Journal of Structural Geology*, 14(10), 1133–1148. [https://doi.org/10.1016/0191-8141\(92\)90065-5](https://doi.org/10.1016/0191-8141(92)90065-5)
- Cowie, P. A., & Scholz, C. H. (1992b). Displacement-length scaling relationship for faults: Data synthesis and discussion. *Journal of Structural Geology*, 14(10), 1149–1156. [https://doi.org/10.1016/0191-8141\(92\)90066-6](https://doi.org/10.1016/0191-8141(92)90066-6)
- Craddock, R. A., & Maxwell, T. A. (1993). Geomorphic evolution of the Martian highlands through ancient fluvial processes. *Journal of Geophysical Research*, 98(E2), 3453–3468. <https://doi.org/10.1029/92JE02508>
- Davis, K., Burbank, D. W., Fisher, D., Wallace, S., & Nobes, D. (2005). Thrust-fault growth and segment linkage in the active Ostler fault zone, New Zealand. *Journal of Structural Geology*, 27(8), 1528–1546. <https://doi.org/10.1016/j.jsg.2005.04.011>
- Dawers, N. H., & Anders, M. H. (1995). Displacement-length scaling and fault linkage. *Journal of Structural Geology*, 17(5), 607–614. [https://doi.org/10.1016/0191-8141\(94\)00091-D](https://doi.org/10.1016/0191-8141(94)00091-D)
- Dawers, N. H., Anders, M. H., & Scholz, C. H. (1993). Growth of normal faults—Displacement-length scaling. *Geology*, 21(12), 1107–1110. [https://doi.org/10.1130/0091-7613\(1993\)021%3C1107:GONFDL%3E2.3.CO;2](https://doi.org/10.1130/0091-7613(1993)021%3C1107:GONFDL%3E2.3.CO;2)
- Edwards, C. S., Nowicki, K. J., Christensen, P. R., Hill, J., Gorelick, N., & Murray, K. (2011). Mosaicking of global planetary image datasets: 1. Techniques and data processing for Thermal Emission Imaging System (THEMIS) multi-spectral data. *Journal of Geophysical Research*, 116, E10008. <https://doi.org/10.1029/2010JE003755>
- Egea-González, I., Jiménez-Díaz, A., Parro, L. M., López, V., Williams, J.-P., & Ruiz, J. (2017). Thrust fault modeling and Late-Noachian lithospheric structure of the circum-Hellas region, Mars. *Icarus*, 288, 53–68. <https://doi.org/10.1016/j.icarus.2017.01.028>
- Elliott, D. (1976). The energy balance and deformation mechanisms of thrust sheets. *Philosophical Transactions of the Royal Society of London, Series A*, 283, 289–312. <https://doi.org/10.1098/rsta.1976.0086>
- Ellis, M. A., & Dunlap, W. J. (1988). Displacement variation along thrust faults: Implications for the development of large faults. *Journal of Structural Geology*, 10(2), 183–192. [https://doi.org/10.1016/0191-8141\(88\)90115-0](https://doi.org/10.1016/0191-8141(88)90115-0)
- Erslev, E. (1986). Basement balancing of Rocky-Mountain foreland uplifts. *Geology*, 14(3), 259–262. [https://doi.org/10.1130/0091-7613\(1986\)14%3C259:BBORMF%3E2.0.CO;2](https://doi.org/10.1130/0091-7613(1986)14%3C259:BBORMF%3E2.0.CO;2)
- Franzke, H. J., Voigt, T., von Eynatten, H., Brix, M. R., & Burmester, G. (2004). Geometrie und Kinematik der Harzrandstörung, erläutert an Profilen aus dem Gebiet von Blankenburg. *Geowissenschaftliche Mitteilungen Thüringen*, 11, 39–62.
- Gillespie, P. A., Walsh, J. J., & Watterson, J. (1992). Limitations of dimension and displacement data from single faults and the consequences for data-analysis and interpretation. *Journal of Structural Geology*, 14(10), 1157–1172. [https://doi.org/10.1016/0191-8141\(92\)90067-7](https://doi.org/10.1016/0191-8141(92)90067-7)
- Golombok, M. P., & Bridges, N. T. (2000). Erosion rates on Mars and implications for climate change: Constraints from the Pathfinder landing site. *Journal of Geophysical Research*, 105(E1), 1841–1853. <https://doi.org/10.1029/1999JE001043>

- Grott, M., Hauber, E., Werner, S. C., Kronberg, P., & Neukum, G. (2007). Mechanical modeling of thrust faults in the Thaumasia region, Mars, and implications for the Noachian heat flux. *Icarus*, 186(2), 517–526. <https://doi.org/10.1016/j.icarus.2006.10.001>
- Hardy, S., & Finch, E. (2005). Discrete element modelling of detachment folding. *Basin Research*, 17(4), 507–520. <https://doi.org/10.1111/j.1365-2117.2005.00280.x>
- Hauck, S. A., Solomon, S. C., & Phillips, R. J. (2003). Potential sources of Hesperian contractional tectonics on Mars, Lunar Planet. Sci. Conf., XXXIV, Abstract 1667.
- Jaeger, J. C., Cook, N. G., & Zimmerman, R. W. (2007). *Fundamentals of rock mechanics* (4th ed. p. 475). Massachusetts: Blackwell Publishing, Malden.
- Johnson, A. M. (1995). Orientations of faults determined by premonitory shear zones. *Tectonophysics*, 247(1-4), 161–238. [https://doi.org/10.1016/0040-1951\(95\)00002-5](https://doi.org/10.1016/0040-1951(95)00002-5)
- Kim, Y.-S., Peacock, D. C. P., & Sanderson, D. J. (2004). Fault damage zones. *Journal of Structural Geology*, 26(3), 503–517. <https://doi.org/10.1016/j.jsg.2003.08.002>
- Kley, J., & Voigt, T. (2008). Late Cretaceous intraplate thrusting in central Europe: Effect of Africa-Iberia-Europe convergence, not Alpine collision. *Geology*, 36(11), 839–842. <https://doi.org/10.1130/G24930A.1>
- Klimczak, C., Schultz, R. A., Parashar, R., & Reeves, D. M. (2010). Cubic law with aperture-length correlation: Implications for network scale fluid flow. *Hydrogeology Journal*, 18(4), 851–862. <https://doi.org/10.1007/s10040-009-0572-6>
- Knapmeyer, M., Oberst, J., Hauber, E., Wählisch, M., Deuchler, C., & Wagner, R. (2006). Working models for spatial distribution and level of Mars' seismicity. *Journal of Geophysical Research*, 111, E11006. <https://doi.org/10.1029/2006JE002708>
- König, S., & Wrede, V. (1994). Zur Tektonik der Harzränder. *Zeitschrift der Deutschen Geologischen Gesellschaft*, 145, 153–171.
- Lavé, J., & Avouac, J. P. (2000). Active folding of fluvial terraces across the Siwaliks Hills, Himalayas of central Nepal. *Journal of Geophysical Research*, 105(B3), 5735–5770. <https://doi.org/10.1029/1999JB900292>
- Lohr, T., Krawczyk, C. M., Oncken, O., Tanner, D. C., Samree, R., Endres, H., et al. (2008). Prediction of subseismic faults and fractures: Integration of three-dimensional seismic data, three-dimensional retro-deformation, and well data on an example of deformation around an inverted fault. *American Association of Petroleum Geologists Bulletin*, 92(4), 473–485. <https://doi.org/10.1306/11260707046>
- Malin, M. C., Bell, J. F. III, Cantor, B. A., Caplinger, M. A., Calvin, W. M., Clancy, R. T., et al. (2007). Context Camera Investigation on board the Mars Reconnaissance Orbiter. *Journal of Geophysical Research*, 112, E05S04. <https://doi.org/10.1029/2006JE002808>
- Mangold, N., Adeli, S., Conway, S., Ansan, V., & Langlais, B. (2012). A chronology of early Mars climatic evolution from impact crater degradation. *Journal of Geophysical Research*, 117, E04003. <https://doi.org/10.1029/2011JE004005>
- Mangold, N., Allemand, P., Thomas, P. G., & Vidal, G. (2000). Chronology of compressional deformation on Mars: Evidence for a single and global origin. *Planetary and Space Science*, 48(12-14), 1201–1211. [https://doi.org/10.1016/S0032-0633\(00\)00104-5](https://doi.org/10.1016/S0032-0633(00)00104-5)
- Manighetti, I., King, G. C. P., Gaudemer, Y., Scholz, C. H., & Doubre, C. (2001). Slip accumulation and lateral propagation of active normal faults in Afar. *Journal of Geophysical Research*, 106(B7), 13,667–13,696. <https://doi.org/10.1029/2000JB900471>
- Marrett, R., & Allmendinger, R. W. (1991). Estimates of strain due to brittle faulting - sampling of fault populations. *Journal of Structural Geology*, 13(6), 735–738. [https://doi.org/10.1016/0191-8141\(91\)90034-G](https://doi.org/10.1016/0191-8141(91)90034-G)
- Matthews, V. (1978). *Laramide folding associated with basement block faulting in the western United States*, Geol. Soc. America, Memoir (Vol. 151, p. 370). Boulder, CO: Geological Society of America.
- Matthews, V., & Work, D. F. (1978, 1978). Laramide folding associated with basement block faulting in the northeastern flank of the Front Range, Colorado. In V. Matthews (Ed.), *Laramide folding associated with basement block faulting in the western United States*, Geol. Soc. America, Memoir (Vol. 151, pp. 101–124). Boulder, CO: Geological Society of America.
- McClay, K. R. (1992). *Thrust Tectonics* (p. 447). Dordrecht, Netherlands: Springer. <https://doi.org/10.1007/978-94-011-3066-0>
- Mitra, S. (1990). Fault-propagation folds: Geometry, kinematic evolution, and hydrocarbon traps. *American Association of Petroleum Geologists Bulletin*, 74, 921–945.
- Mueller, K., Vidal, A., Robbins, S., Golombek, M., & West, C. (2014). Fault and fold growth of the Amenthes uplift: Implications for Late Noachian crustal rheology and heat flow on Mars. *Earth and Planetary Science Letters*, 408, 100–109. <https://doi.org/10.1016/j.epsl.2014.09.047>
- Nahm, A. L., & Schultz, R. A. (2011). Magnitude of global contraction on Mars from analysis of surface faults: Implications for Martian thermal history. *Icarus*, 211(1), 389–400. <https://doi.org/10.1016/j.icarus.2010.11.003>
- Neukum, G., Greeley, R., Hiesinger, H., & Pinet, P. (2010). Mars geology from three – Dimensional mapping by the High Resolution Stereo Camera (HRSC) Experiment on Mars Express. An introduction to the special issue of Earth Planetary Science Letters. *Earth and Planetary Science Letters*, 294(3-4), 183–184. <https://doi.org/10.1016/j.epsl.2010.04.040>
- Nicol, A., Waterson, J., Walsh, J. J., & Childs, C. (1996). The shapes, major axis orientations and displacement patterns of fault surfaces. *Journal of Structural Geology*, 18(2–3), 235–248. [https://doi.org/10.1016/S0191-8141\(96\)80047-2](https://doi.org/10.1016/S0191-8141(96)80047-2)
- Okubo, C. H., & Schultz, R. A. (2004). Mechanical stratigraphy in the western equatorial region of Mars based on thrust fault-related fold topography and implications for near-surface volatile reservoirs. *Geological Society of America Bulletin*, 116(5), 594. <https://doi.org/10.1130/B25361.1>
- Peacock, D. C. P. (1991). Displacement and segment linkage in strike-slip fault zones. *Journal of Structural Geology*, 13(9), 1025–1035. [https://doi.org/10.1016/0191-8141\(91\)90054-M](https://doi.org/10.1016/0191-8141(91)90054-M)
- Polit, A. T., Schultz, R. A., & Soliva, R. (2009). Geometry, displacement-length scaling, and extensional strain of normal faults on Mars with inferences on mechanical stratigraphy of the Martian crust. *Journal of Structural Geology*, 31(7), 662–673. <https://doi.org/10.1016/j.jsg.2009.03.016>
- Ray, S. K. (2006). Scaling properties of thrust fault traces in the Himalayas and inferences on thrust fault growth. *Journal of Structural Geology*, 28(7), 1307–1315. <https://doi.org/10.1016/j.jsg.2006.02.010>
- Robbins, S. J., & Hynek, B. M. (2012). A new global database of Mars impact craters ≥ 1 km: 1. Database creation, properties, and parameters. *Journal of Geophysical Research*, 117, E05004. <https://doi.org/10.1029/2011JE003966>
- Ruiz, J., Fernández, C., Gomez-Ortiz, D., Dohm, J. M., López, V., & Tejero, R. (2008). Ancient heat flow, crustal thickness, and lithospheric mantle rheology in the Amenthes region, Mars. *Earth and Planetary Science Letters*, 270(1–2), 1–12. <https://doi.org/10.1016/j.epsl.2008.02.015>
- Schlische, R. W., Young, S. S., Ackermann, R. V., & Gupta, A. (1996). Geometry and scaling relations of a population of very small rift-related normal faults. *Geology*, 24(8), 683–686. [https://doi.org/10.1130/0091-7613\(1996\)024%3C0683:GARSOA%3E2.3.CO;2](https://doi.org/10.1130/0091-7613(1996)024%3C0683:GARSOA%3E2.3.CO;2)
- Schultz, R. A. (2000). Localization of bedding plane slip and backthrust faults above blind thrust faults: Keys to wrinkle ridge structure. *Journal of Geophysical Research*, 105(E5), 12,035–12,052. <https://doi.org/10.1029/1999JE001212>
- Schultz, R. A. (2003a). A method to relate initial elastic stress to fault population strains. *Geophysical Research Letters*, 30(11), 1593. <https://doi.org/10.1029/2002GL016681>

- Schultz, R. A. (2003b). Seismotectonics of the Amenthes Rupes thrust fault population, Mars. *Geophysical Research Letters*, 30(6), 1303. <https://doi.org/10.1029/2002GL016475>
- Schultz, R. A., & Fossen, H. (2002). Displacement-length scaling in three dimensions: The importance of aspect ratio and application to deformation bands. *Journal of Structural Geology*, 24(9), 1389–1411. [https://doi.org/10.1016/S0191-8141\(01\)00146-8](https://doi.org/10.1016/S0191-8141(01)00146-8)
- Schultz, R. A., Okubo, C. H., & Wilkins, S. J. (2006). Displacement-length scaling relations for faults on the terrestrial planets. *Journal of Structural Geology*, 28(12), 2182–2193. <https://doi.org/10.1016/j.jsg.2006.03.034>
- Schultz, R. A., Soliva, R., Okubo, C., & Mege, D. (2010). Fault populations. In T. R. Watters & R. A. Schultz (Eds.), *Planetary tectonics* (pp. 457–510). Cambridge, UK: Cambridge University Press.
- Schultz, R. A., & Watters, T. R. (2001). Forward mechanical modeling of the Amenthes Rupes thrust fault on Mars. *Geophysical Research Letters*, 28(24), 4659–4662. <https://doi.org/10.1029/2001GL013468>
- Shaw, J. H., Connors, C., & Suppe, J. (2005). Seismic interpretation of contractional fault-related folds, An AAPG seismic atlas. *AAPG Studies in Geology*, 53, 156.
- Shaw, J. H., Plesch, A., Dolan, J. F., Pratt, T. L., & Fiore, P. (2002). Puente Hills blind-thrust system, Los Angeles, California. *Bulletin of the Seismological Society of America*, 92(8), 2946–2960. <https://doi.org/10.1785/0120010291>
- Sibson, R. H. (1986). Rupture interaction with fault jogs. In S. Das, J. Boatwright, & C. H. Scholz (Eds.), *Earthquake source mechanics*, AGU Geophysical Monograph, Maurice Ewing Series (Vol. 6, pp. 157–167).
- Soliva, R., & Benedicto, A. (2005). Geometry, scaling relations and spacing of vertically restricted normal faults. *Journal of Structural Geology*, 27(2), 317–325. <https://doi.org/10.1016/j.jsg.2004.08.010>
- Soliva, R., Benedicto, A., & Maerten, L. (2006). Spacing and linkage of confined normal faults: Importance of mechanical thickness. *Journal of Geophysical Research*, 111, B01402. <https://doi.org/10.1029/2004JB003507>
- Soliva, R., Schultz, R. A., & Benedicto, A. (2005). Three-dimensional displacement-length scaling and maximum dimension of normal faults in layered rocks. *Geophysical Research Letters*, 32, L16302. <https://doi.org/10.1029/2005GL023007>
- Solomon, S. C., & Chaiken, J. (1976). Thermal expansion and thermal stress in the Moon and terrestrial planets: Clues to early thermal history. *Proceedings of the Lunar and Planetary Science Conference*, 7, 3229–3243.
- Stackebrandt, W. (1983). Zum tektonischen Charakter der Harznordrandstörung, Ver. Zent. Ph. 77, 187–193.
- Stone, D. S. (1993). Basement-involved thrust-generated folds as seismically imaged in the subsurface of the central Rocky Mountain foreland. *Geological Society of America Special Papers*, 280, 271–318.
- Suppe, J., & Medwedeff, D. A. (1990). Geometry and kinematics of fault-propagation folding. *Elogiae Geologicae Helveticae*, 83(3), 409–454.
- Trudgill, B., & Cartwright, J. (1994). Relay-ramp forms and normal-fault linkages, Canyonlands National Park, Utah. *Geological Society of America Bulletin*, 106(9), 1143–1157. [https://doi.org/10.1130/0016-7606\(1994\)106%3C1143:RRFANF%3E2.3.CO;2](https://doi.org/10.1130/0016-7606(1994)106%3C1143:RRFANF%3E2.3.CO;2)
- van Gasselt, S., Rossi, A. P., Orgel, C., & Schultz, J. (2015). Phlegra Montes, Mars: Chronology and Denudation Rates, Lunar Planetary Science Conf., XLVI, abstract 1371.
- Walsh, J. J., & Watterson, J. (1987). Distributions of cumulative displacement and seismic slip on a single normal-fault surface. *Journal of Structural Geology*, 9(8), 1039–1046. [https://doi.org/10.1016/0191-8141\(87\)90012-5](https://doi.org/10.1016/0191-8141(87)90012-5)
- Walsh, J. J., & Watterson, J. (1988). Analysis of the relationship between displacements and dimensions of faults. *Journal of Structural Geology*, 10(3), 239–247. [https://doi.org/10.1016/0191-8141\(88\)90057-0](https://doi.org/10.1016/0191-8141(88)90057-0)
- Walsh, J. J., & Watterson, J. (1991). Geometric and kinematic coherence and scale effects in normal fault systems. In A. M. Roberts, G. Yielding, & B. Freeman (Eds.), *The geometry of normal faults*, Geological Society of London, Special Publication (Vol. 56, pp. 193–203).
- Watters, T. R. (1993). Compressional tectonism on Mars. *Journal of Geophysical Research*, 98(E9), 17,049–17,060. <https://doi.org/10.1029/93JE01138>
- Watters, T. R. (2003a). Lithospheric flexure and the origin of the dichotomy boundary on Mars. *Geology*, 33(8), 271–274. <https://doi.org/10.1029/2005GL024325>
- Watters, T. R. (2003b). Thrust faults along the dichotomy boundary in the eastern hemisphere of Mars. *Journal of Geophysical Research*, 108(E6), 5054. <https://doi.org/10.1029/2002JE001934>
- Watters, T. R. (2004). Elastic dislocation modeling of wrinkle ridges on Mars. *Icarus*, 171(2), 284–294. <https://doi.org/10.1016/j.icarus.2004.05.024>
- Watters, T. R., & Robinson, M. S. (1999). Lobate scarps and the Martian crustal dichotomy. *Journal of Geophysical Research*, 104(E8), 18,981–18,990. <https://doi.org/10.1029/1998JE001007>
- Watters, T. R., Schultz, R. A., & Robinson, M. S. (2000). Displacement-length relations of thrust faults associated with lobate scarps on Mercury and Mars: Comparison with terrestrial faults. *Geophysical Research Letters*, 27(22), 3659–3662. <https://doi.org/10.1029/2000GL011554>
- Watterson, J. (1986). Fault dimensions, displacements and growth. *Pure and Applied Geophysics*, 124(1–2), 365–373. <https://doi.org/10.1007/BF00875732>
- Wickham, J. (1995). Fault displacement-gradient folds and the structure at Lost Hills, California. *Journal of Structural Geology*, 17(9), 1293–1302. [https://doi.org/10.1016/0191-8141\(95\)00029-D](https://doi.org/10.1016/0191-8141(95)00029-D)
- Willemse, E. J. M. (1997). Segmented normal faults: Correspondence between three-dimensional mechanical models and field data. *Journal of Geophysical Research*, 102(B1), 675–692. <https://doi.org/10.1029/96JB01651>
- Willemse, E. J. M., Pollard, D. D., & Aydin, A. (1996). 3D analyses of slip distributions on normal fault arrays with consequences for fault scaling. *Journal of Structural Geology*, 18(2–3), 295–309. [https://doi.org/10.1016/S0191-8141\(96\)80051-4](https://doi.org/10.1016/S0191-8141(96)80051-4)
- Williams, G., & Chapman, T. (1983). Strains developed in the hanging walls of thrusts due to their slip/propagation rate: A dislocation model. *Journal of Structural Geology*, 5(6), 563–571. [https://doi.org/10.1016/0191-8141\(83\)90068-8](https://doi.org/10.1016/0191-8141(83)90068-8)
- Wyrick, D. Y., Morris, A. P., & Ferrill, D. A. (2011). Normal fault growth in analog models and on Mars. *Icarus*, 212(2), 559–567. <https://doi.org/10.1016/j.icarus.2011.01.011>
- Yin, A. (2012). An episodic slab-rollback model for the origin of the Tharsis rise on Mars: Implications for initiation of local plate subduction and final unification of a kinematically linked global plate-tectonic network on Earth. *Lithosphere*, 4(6), 553–593. <https://doi.org/10.1130/L195.1>
- Zehnder, A. T., & Allmendinger, R. W. (2000). Velocity field for the trishear model. *Journal of Structural Geology*, 22(8), 1009–1014. [https://doi.org/10.1016/S0191-8141\(00\)00037-7](https://doi.org/10.1016/S0191-8141(00)00037-7)
- Ziegler, P. A., Cloetingh, S., & van Wees, J.-D. (1995). Dynamics of intra-plate compressional deformation: The Alpine foreland and other examples. *Tectonophysics*, 252(1–4), 7–59. [https://doi.org/10.1016/0040-1951\(95\)00102-6](https://doi.org/10.1016/0040-1951(95)00102-6)
- Zuber, M. T. (2001). The crust and mantle of Mars. *Nature*, 412(6843), 220–227. <https://doi.org/10.1038/35084163>